

# Using Temporal Deep Learning Models to Estimate Historical and End-Century Daily Snow Water Equivalent over the Rocky Mountains

Shiheng Duan<sup>1</sup>, Paul Ullrich<sup>2</sup>, Mark Risser<sup>3</sup>, and Alan Rhoades<sup>3</sup>

<sup>1</sup>University of California, Davis

<sup>2</sup>University of California Davis

<sup>3</sup>Lawrence Berkeley National Laboratory

March 31, 2023

1      **Using Temporal Deep Learning Models to Estimate  
2      Daily Snow Water Equivalent over the Rocky  
3      Mountains**

4      **Shiheng Duan<sup>1</sup>, Paul Ullrich<sup>1</sup>, Mark Risser<sup>2</sup>, Alan Rhoades<sup>2</sup>**

5      <sup>1</sup>Atmospheric Science Graduate Group, University of California, Davis  
6      <sup>2</sup>Lawrence Berkeley National Laboratory

7      **Key Points:**

- 8      • Three different deep learning models are assessed for daily snow water equivalent  
9      prediction.  
10     • Sensitivity tests provide evidence the DL models follow physical laws.  
11     • Snow water equivalent fraction is used to alleviate problems with spatial extrapolation.  
12

13 **Abstract**

14 In this study we construct and compare three different deep learning (DL) models for  
 15 estimating daily snow water equivalent (SWE) from high-resolution gridded meteorological  
 16 fields over the Rocky Mountain region. To train the DL models, Snow Telemetry (SNOWTEL)  
 17 station-based SWE observations are used as the prediction target. All  
 18 DL models produce higher median Nash-Sutcliffe Efficiency (NSE) values than a process-  
 19 based SWE model and products, although mean squared errors also tend to be higher.  
 20 Sensitivity of the SWE prediction to the model's input variables is analyzed using an ex-  
 21 plainable artificial intelligence (XAI) method, yielding insight into the physical relation-  
 22 ships learned by the models. This method reveals the dominant role precipitation and  
 23 temperature play in snowpack dynamics. In applying our models to estimate SWE through-  
 24 out the Rocky Mountains, an extrapolation problem arises since the statistical proper-  
 25 ties of SWE (e.g., annual maximum) and geographical properties of individual grid points  
 26 (e.g., elevation) differ from the training data. This problem is solved by switching the  
 27 prediction target to SWE fraction to alleviate extrapolation for all tested DL models.  
 28 Our work shows that the DL models are promising tools for estimating SWE, and suf-  
 29 ficiently capture relevant physical relationships to make them useful for spatial and tem-  
 30 poral extrapolation of SWE values.

31 **1 Introduction**

32 Snowpack is a central component of the hydrologic cycle in montane regions, and  
 33 its capacity to act as a reservoir for seasonal water storage is of vital importance to down-  
 34 stream communities. This is especially true for watersheds in mid-to-high latitudes and  
 35 at altitudes where streamflow is derived largely from snowmelt (Berghuijs et al., 2019).  
 36 Snow water equivalent (SWE), defined as the equivalent amount of liquid water stored  
 37 in the snowpack if it were to be instantaneously melted, is the metric most commonly  
 38 employed by water managers to estimate and evenly compare water content of the snow-  
 39 pack across regions. Climate change has already and will continue to significantly reduce  
 40 both mean and maximum annual SWE, which will have repercussions for both stream-  
 41 flow and groundwater dynamics, and in turn pose major challenges on water managers  
 42 (Rhoades, Ullrich, & Zarzycki, 2018; Livneh & Badger, 2020; X. Chen et al., 2021; Hatch-  
 43 ett et al., 2022; Rhoades et al., 2022). However, estimating the exact magnitude, tim-  
 44 ing and persistence of SWE across various mountain ranges remains a scientific grand  
 45 challenge (Siirila-Woodburn et al., 2021). Thus, there is considerable value for both sci-  
 46 ence and society in the development of novel methods that can more precisely estimate  
 47 spatiotemporally continuous SWE values over mountainous regions, both historically and  
 48 into the future.

49 Substantial and rapid progress in the development of machine learning (ML) and  
 50 deep learning (DL) methods, and corresponding hardware advancements related to graph-  
 51 ical processing units (GPUs), has stimulated promising research in the use of ML and  
 52 DL-based models for problems in Earth system science (Feng et al., 2022). ML models  
 53 have also been employed and have proven valuable for estimating SWE, although the  
 54 majority of this research has focused on historical SWE estimation from existing snow  
 55 and snow-related datasets. For instance, Snauffer et al. (2018) used an artificial neural  
 56 network (ANN) model to estimate SWE from several reanalysis products. Their ML-  
 57 generated SWE estimation exhibited better agreement with station observations, com-  
 58 pared to those derived from a Variable Infiltration Capacity (VIC) hydrological model  
 59 simulation. Odry et al. (2020) and Ntokas et al. (2021) designed an ANN model to pre-  
 60 dict SWE and demonstrated that their ML model outperformed the benchmark regres-  
 61 sion model. Their input variables included snow depth, temperature, accumulated pre-  
 62 cipitation and several indices such as the number of snow-free days and the number of  
 63 layers in the snowpack. Random forest methods have also been adopted to bias correct  
 64 gridded SWE products (King et al., 2020).

To date, ML-based SWE estimation has largely relied on inference or emulation of existing snow-related products, rather than accounting for physical processes that shape snow accumulation. However, recent work by Manepalli et al. (2019) used a conditional generative adversarial network (cGAN) to emulate VIC-based estimates of SWE developed by Livneh et al. (2015). They formulated this task as an image-to-image translation problem, where the cGAN model translates gridded relationships between the input meteorological fields to the target SWE field without the need for snow-related products. Although the cGAN model is demonstrably powerful, this type of image translation task does not allow time dependency to be incorporated into the model. Namely, it assumes the SWE at time  $t$  can be expressed as a function of meteorological variables at the concurrent time  $t$ . Under such an architecture, the model cannot capture temporal features from the input predictors, (i.e., the snow accumulation process is ignored), which is vital for time series prediction.

There have also been recent efforts to estimate SWE based on precipitation ( $P$ ), temperature ( $T$ ) and other factors that leverage physical causation and a process-based understanding of the system. These new DL models have modeled SWE as an accumulation process by relating SWE to a historic time series of meteorological variables, with the inputs from previous time steps:

$$\text{SWE}_t = f(P_t, P_{t-1}, \dots, P_{t-N+1}, T_t, T_{t-1}, \dots, T_{t-N+1}) \quad (1)$$

where  $t$  denotes the time step and  $N$  is the length of the look-back window size. Using the above formula, Meyal et al. (2020) inputted precipitation, temperature, snow depth and SWE from previous days into a long-short-term memory (LSTM) model for SWE prediction at five observational stations. They found that the LSTM model can capture the temporal features of snow accumulation and perform well at the selected stations. Similarly, in Y.-H. Wang et al. (2022) an LSTM model is trained to emulate a gridded SWE dataset, demonstrating the superior ability of LSTM to capture snowpack dynamics over the western US. In these studies, both Manepalli et al. (2019) and Y.-H. Wang et al. (2022) emulated existing SWE products, while Meyal et al. (2020) used observational records and thus did not assume the quality of any existing model or dataset.

Although ML and DL models can achieve satisfying results for historical SWE, models generally struggle with poor performance under extrapolation. Although the LSTM model in Meyal et al. (2020) performed well at the selected observational sites, it was not tested in out-of-sample areas, especially where the statistical properties of SWE accumulation are different from the training sites. This poses a major challenge, particularly if we want to generate a gridded SWE dataset with ML or DL models trained on in-situ observations. Given that in-situ estimates of SWE are generally located in those mountainous areas that are easily accessible and found at mid-elevation, they do not fully represent the areal heterogeneity of SWE at high-elevation or low-elevation that surround the stations (Blöschl, 1999). Therefore, a significant extrapolation problem may arise, particularly when applying the ML or DL models to low-elevation plains or valleys. This issue also makes it difficult to validate or calibrate process-based models, suggesting a need for more observations at both low- and high-elevation. In the case of ML-based models, efforts to address the extrapolation problem include a transformation of the output target for climate emulation or by evaluating model performance using (extreme) out-of-sample scenarios for streamflow projection (S. Duan et al., 2020; Beucler, Pritchard, Rasp, et al., 2021).

In our study, we investigate the viability of DL models for modeling SWE at pointwise locations and as a gridded product. Such datasets would have significant value to both researchers and practitioners, particularly those invested in water resource availability and management. We first build three DL models based on equation (1), only using the meteorological forcings from 581 observational stations in the western United States (WUS). The model behavior and input sensitivity are subsequently analyzed using an

116 explainable artificial intelligence (XAI) method. With these trained DL models in hand,  
 117 we then tackle the spatial extrapolation problem and generate a gridded SWE product  
 118 over the Rocky Mountains with 4km grid spacing. This work further sets the stage for  
 119 a successive effort to leverage our DL model for predicting the response of mountain snow-  
 120 pack to climate change.

121 The structure of this paper is as follows. Section 2 describes the models employed,  
 122 the data sources used in our study, and methods for analysis. Section 3 provides a com-  
 123 parative assessment of model performance, including model behavior under cross-validation,  
 124 and a permutation-based analysis of the DL model to understand which variables are  
 125 deemed most relevant for SWE prediction. The DL model is then extnded to generate  
 126 a gridded SWE product, which is described and analyzed in section 4. A discussion of  
 127 DL model performance in contrast with a process-based model are in section 5, followed  
 128 by conclusions in section 6.

## 129 2 Models, Data and Methods

### 130 2.1 Deep Learning Models

131 Three different DL models applicable to time series problems are investigated and  
 132 compared, following the general framework depicted in Figure 1. Under this design, the  
 133 temporal block extracts temporal features from the input data, while the dense layer gen-  
 134 erates a single-step prediction. The DL models are trained to minimize an objective func-  
 135 tion (i.e., the loss function), which in this study is chosen to be the mean squared error  
 136 (MSE). The number of training periods (epochs) is set to 50. The optimization algorithm  
 137 is Adam with a learning rate of 1e-4 (Kingma & Ba, 2014). Since a gradient-based method  
 138 is used to optimize the DL model, the converged model will be sensitive to the choice  
 139 of initial weights. This effect is mitigated by training models 10 times with different ini-  
 140 tial weights to generate an ensemble of predictions and use the ensemble mean, follow-  
 141 ing X. Wang et al. (2021). The remaining hyperparameters for each model architecture  
 142 are determined by grid search (more details in Appendix Appendix B). Hyperparam-  
 143 meters are not fine-tuned in this study due to the steep computational cost and the min-  
 144 imal benefit awarded by such an approach. All DL models are implemented using Py-  
 145 Torch (Paszke et al., 2019). Specific details on the three DL models, along with our de-  
 146 sign choices, are as follows.

#### 147 2.1.1 Long-Short Term Memory (*LSTM*)

148 Long-Short Term Memory models (LSTMs) (Hochreiter & Schmidhuber, 1997) are  
 149 a type of recurrent neural network that has commonly been used in hydrological predic-  
 150 tion (Kratzert et al., 2019a; Feng et al., 2020; Lees et al., 2021). LSTMs have demon-  
 151 strated considerable success for problems of this type, since they are designed to cap-  
 152 ture temporal dependencies that are common in time-series data.

153 Details on the mathematical structure of the LSTM are provided in Text S1. The  
 154 gated design of LSTM enables it to keep and drop information from the previous time  
 155 steps, which is naturally suited for time series tasks. A detailed figure representing the  
 156 gates and outputs is depicted in Figure S1. Theoretically, there can be multiple LSTM  
 157 layers stacked in a single LSTM model. However, the majority of past hydrological ap-  
 158 plication studies adopt a one-layer LSTM model (Kratzert et al., 2019a; Xiang et al., 2020;  
 159 Feng et al., 2020; Wunsch et al., 2021). In this study, we also utilize a one-layer LSTM  
 160 model with the number of hidden units (i.e., the dimension of cell state) selected by hy-  
 161 perparameter search.

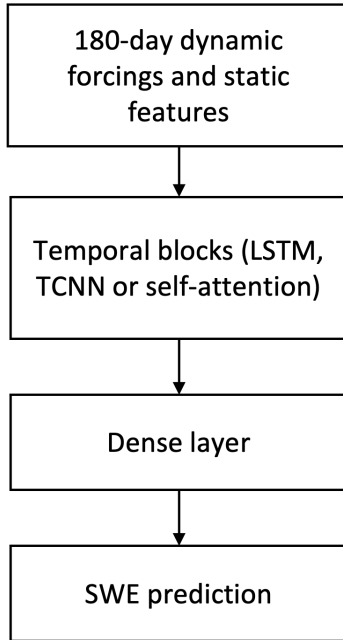


**Figure 1.** The general framework employed in this study for all ML models.

162

### 2.1.2 Temporal Convolutional Neural Network (TCNN)

163  
164  
165  
166  
167  
168  
169  
170  
171  
172  
173

Historically, convolutional models have been used for image-related tasks because of their ability to extract features with 2- or 3-dimensional convolutional kernels (i.e., weighted inner products that are marched across the input image). Two well-known image-related models built with convolution layers are VGG-16 (Simonyan & Zisserman, 2014) and GoogLeNet (Szegedy et al., 2015). Temporal convolutional neural networks (TCNNs) (Lea et al., 2017), where kernels are instead applied over the time dimension, have also been developed for time-series problems. Bai et al. (2018) tested these models for a variety of standard time series tasks and showed that convolutional models can often outperform LSTMs. TCNNs have also been used in Earth system modelling for predictions of streamflow and the El Niño Southern Oscillation (ENSO) (S. Duan et al., 2020; Yan et al., 2020).

174  
175  
176  
177  
178  
179  
180  
181  
182  
183

To mimic the inherent time dependencies built into LSTMs, TCNNs use dilated causal convolutions and residual connections (Bai et al., 2018). This architecture is depicted in Figure S2. The causal convolution ensures that outputs at a given time step are only dependent on previous time steps, in contrast to a traditional convolution which could involve future information. The dilated convolution enlarges the receptive field by regularly skipping input time steps; consequently, with stacked deep CNN layers, the receptive field at the final layer can cover the whole input time series. Residual connections are needed along with the stacked layers since the model can be too deep to converge, and residual connections can avoid vanishing or exploding gradients (K. He et al., 2016).

184  
185  
186  
187

In this study, we use a stacked TCNN model analogous to those employed in Bai et al. (2018) and S. Duan et al. (2020), where each TCNN block consists of two CNN layers and one residual connection (Figure S2). The number of CNN kernels, TCNN blocks and kernel sizes are determined by hyperparameter search.

188      **2.1.3 Self-Attention Model**

189      Vaswani et al. (2017) introduced the Transformer, a self-attention based encoder-  
 190      decoder model (Bahdanau et al., 2014) for natural language processing (NLP). Since then,  
 191      many self-attention-based models have been designed and investigated for application  
 192      to time series problems (Devlin et al., 2018). In Earth system modeling applications, self-  
 193      attention-based models have been used to predict the ENSO index (Ye et al., 2021) and  
 194      forecast seasonal precipitation (Civitarese et al., 2021). In recent years, significant ef-  
 195      fort has been made to optimize the original Transformer architecture and make it more  
 196      computationally and memory efficient (Tay et al., 2020; Lin et al., 2021). These variants  
 197      of Transformer models could provide more choices for Earth system applications.

198      The equations governing the self-attention model are provided in Text S1. In the  
 199      encoder portion of Transformer, the input vectors are embedded in a dense layer (also  
 200      called an embedding layer). The self-attention layer takes the embedded inputs and ex-  
 201      tracts the temporal features, which are then used as input for the decoder (depicted in  
 202      Figure S3). It can be viewed as a fully connected layer but with dynamical weights rep-  
 203      resenting the pairwise relationships of the input time steps (Lin et al., 2021).

204      In this study, the encoder of the original Transformer model from Vaswani et al.  
 205      (2017) is used, featuring a multi-head self-attention mechanism. The number of Trans-  
 206      former encoder layers, number of heads, embedding size and feedforward dimensions are  
 207      tuned using a hyperparameter search.

208      **2.2 Training Data**

209      Snow Telemetry (SNOTEL) stations provide daily SWE measurements and are used  
 210      as the prediction target for the ML model. From the 829 stations with available data  
 211      (including Alaska), we select 581 stations across the WUS with at least one year of com-  
 212      plete observations over the training period from 1980 to 1990. Meteorological fields are  
 213      from the 1/24th-degree ( $\sim 4\text{-km}$ ) gridMET dataset, including daily precipitation, max-  
 214      imum and minimum temperature, solar radiation, maximum and minimum relative hu-  
 215      midity, specific humidity, vapor deficit and wind speed (Abatzoglou, 2013). Since SNO-  
 216      TEL stations do not coincide with gridMET grid points, the data point nearest to each  
 217      SNOTEL station provides the corresponding forcing.

218      Static features at each station include latitude, longitude, elevation, diurnal anisotropic  
 219      heat index (DAH) (Böhner & Antonić, 2009) and topographic solar radiation aspect in-  
 220      dex (TRASP) (Roberts & Cooper, 1989). DAH and TRASP are used to account for sur-  
 221      face solar radiation loading (i.e., shading) (Cristea et al., 2017). DAH is given by

$$\text{DAH} = \cos(\alpha_{\max} - \alpha) \times \arctan(\beta) \quad (2)$$

222      where  $\alpha_{\max}$  is the aspect receiving the maximum amount of solar radiation (for the WUS,  
 223      we use  $\alpha_{\max} = 1.125\pi$ , following Böhner and Antonić (2009)),  $\alpha$  is the aspect (in ra-  
 224      dians), and  $\beta$  is the topographic slope (also in radians). DAH ranges between  $-1$  and  
 225       $+1$ , with zero corresponding to flat terrain; for the WUS, DAH is largest on steep southwest-  
 226      facing slopes that have higher afternoon solar radiation loading and lowest on steep north-  
 227      facing slopes. TRASP is given by

$$\text{TRASP} = \frac{1}{2} \left[ 1 - \cos \left( \alpha - \frac{\pi}{6} \right) \right]. \quad (3)$$

228      TRASP is only a function of topographic aspect and accounts for daily solar radiation  
 229      loading and ranges between  $0$  (for the coolest slopes) and  $+1$  (for the warmest slopes).  
 230      Both TRASP and DAH were calculated using the United States Geological Survey (USGS)  
 231      Digital Elevation Model (DEM) dataset at 30-meter horizontal resolution. As with grid-  
 232      MET, the nearest grid cell to the SNOTEL station is used as the corresponding input  
 233      to the DL model.

234            **2.3 Splitting the Data**

235        For purposes of constructing the primary DL models, the data are split into training,  
 236        validation and testing sets. Several such splittings are used throughout our paper  
 237        in order to test the robustness of the DL method for capturing snowpack dynamics among  
 238        different time periods and in different regions. For all splittings, we calculate the mean  
 239         $\bar{x}$  and standard deviation  $\sigma$  of both the input and output variables in the training pe-  
 240        riod and so normalize the data via

$$X_{\text{normalized}} = \frac{x_i - \bar{x}}{\sigma}. \quad (4)$$

241        The splittings employed are as follows:

- 242        (1) For the temporal train-test split, we use 1980 Oct 1st to 1999 Sep 30th as the train-  
       243        ing period, 1999 Oct 1st to 2008 Sep 30th as the validation period and 2008 Oct  
       244        1st to 2018 Sep 30th as the testing period. All SNOTEL stations are included in  
       245        this splitting. Since validation is only used to determine hyper-parameters (which  
       246        are fixed thereafter), this is the only splitting that includes a validation period.
- 247        (2a) For the first spatial train-test split, SNOTEL stations are split into eight moun-  
       248        tain ranges, including the Pacific Northwest, the Sierra Nevada, the Blue Moun-  
       249        tains, Idaho/Western Montana, Northwestern Wyoming, Utah, Colorado, and Ari-  
       250        zona/New Mexico. This division follows Serreze et al. (1999) and M. He et al. (2011b),  
       251        where it was shown that these eight mountain ranges exhibited distinct snow dy-  
       252        namics. This splitting includes eight experiments, in each case using seven moun-  
       253        tain ranges for training and one for testing.
- 254        (2b) For the second spatial train-test split, all SNOTEL stations are randomly split into  
       255        eight subsets or folds. Each time this splitting is performed, seven folds are used  
       256        for training and the rest for testing. Unlike the spatial splitting in (2a), this spa-  
       257        tial splitting still allows the model to comprehensively learn snow dynamics from  
       258        throughout the western US.

259            **2.4 Gridded SWE Reference Products**

260        Spatiotemporally complete observations of SWE in mountain areas remain elusive,  
 261        requiring us to instead employ reconstructions that meld models and observations. Of  
 262        course, such products inevitably inherit biases from incomplete observations and uncer-  
 263        tainties in the model design, particularly in regions where observations are sparse. To  
 264        better quantify these structural uncertainties, two model products are employed in this  
 265        study. These two products were chosen because they are modern, high-quality data prod-  
 266        ucts that are widely used in the snow modeling community. Other such SWE products  
 267        can be found in McCrary et al. (2017) and Snauffer et al. (2018).

268        The primary product employed is the daily 4km gridded SWE data from Zeng et  
 269        al. (2018) (hereafter referred to as the University of Arizona or UA dataset), which uses  
 270        PRISM precipitation and temperature data and assimilates SNOTEL observations. In  
 271        the UA product, rainfall and snowfall are partitioned using daily 2m air temperature thresh-  
 272        olds derived from station observations. When interpolating point measurements to a grid,  
 273        the ratio of SWE observations is used instead of the absolute SWE measurements as net  
 274        snowfall was found to be overestimated. Further details on the methodology employed  
 275        and corresponding analysis can be found in Broxton et al. (2016) and Zeng et al. (2018).

276        The second product adopted in this study is an independent SWE dataset devel-  
 277        oped at the University of California, Los Angeles, (referred to as the UCLA dataset). The  
 278        UCLA dataset takes three Landsat sensors as input, along with meteorological forcings,  
 279        topographical features and landcover data. The snow estimates are then updated with  
 280        MODIS remote sensing estimates of snow cover too. Within a Bayesian framework, this  
 281        dataset provides ensemble statistics of SWE estimates (e.g., mean, standard deviation,

median) (Y. Fang et al., 2022). Details about the processing algorithm can be found at Margulis et al. (2019). The horizontal resolution of the UCLA product is 16 arc seconds, which varies from 350m to 500m. For the purposes of this study we use the ensemble mean SWE estimate, which is regridded to the same 4km resolution grid as the UA dataset.

## 286 2.5 The SNOW-17 Model

287 One issue with the use of gridded products is that they do not provide SWE data  
 288 at the precise SNOTEL station locations. Interpolating meteorological and SWE data  
 289 from gridded data points to SNOTEL stations can introduce potentially significant er-  
 290 rors, particularly in regions of complex topography. Consequently, we further compare  
 291 our DL-based SWE estimates to those from the process-based SNOW-17 snow accumu-  
 292 lation and ablation model. SNOW-17 uses an air temperature index to determine en-  
 293 ergy exchanges at the snow-air interface and enforces principles of water and energy bal-  
 294 ance to estimate SWE and runoff. We refer readers to E. A. Anderson (1976) and E. An-  
 295 derson (2006) for the detailed processes and equations used in the SNOW-17 model.

296 Training data from selected SNOTEL stations and gridMET are used to calibrate  
 297 the SNOW-17 model (i.e., 1980 Oct 1st to 1999 Sep 30th). The model is then used to  
 298 generate SWE estimates over the testing period (2008 Oct 1st to 2018 Sep 30th) for com-  
 299 parison. Candidate tuning parameters are determined based on previous studies on model  
 300 sensitivities (e.g., E. A. Anderson, 1973; M. He et al., 2011a; Raleigh & Lundquist, 2012)  
 301 and listed in the Appendix. The shuffled complex evolution approach (SCE-UA) is used  
 302 to optimize the parameters, with details in Q. Duan et al. (1993, 1994).

## 303 2.6 Performance Metrics

304 Model performance is quantified using the Nash-Sutcliffe model efficiency coeffi-  
 305 cient (NSE), a widely used metric for hydrological model evaluation (Nash & Sutcliffe,  
 306 1970). It is defined via

$$\text{NSE}(O_t, P_t) = 1 - \frac{\sum(O_t - P_t)^2}{\sum(\bar{O}_t - O_t)^2}, \quad (5)$$

307 where  $O$  and  $P$  denote observations and predictions, respectively. Index  $t$  denotes the  
 308 time and  $\bar{O}_t$  is the observation mean. NSE is in the range  $(-\infty, 1]$ , with larger values  
 309 indicating better performance and a score of 1 indicating a perfect match between model  
 310 and observations. Note that the NSE score is not symmetric, i.e.,  $\text{NSE}(A, B) \neq \text{NSE}(B, A)$ ;  
 311 in this study the first NSE argument consistently refers to the reference product.

312 In this study, we employ NSE in two ways. First, the NSE of absolute SWE is cal-  
 313 culated as

$$\text{NSE}_{\text{absolute}} = \text{NSE}(\text{SWE-REF}, \text{SWE-DL}), \quad (6)$$

314 where SWE-REF denotes the SWE from the reference dataset and SWE-DL denotes the  
 315 SWE prediction from the deep learning model. Second, the NSE of the SWE fraction  
 316 is given by

$$\text{NSE}_{\text{fraction}} = \text{NSE}\left(\frac{\text{SWE-REF}}{\max(\text{SWE-REF})}, \frac{\text{SWE-DL}}{\max(\text{SWE-DL})}\right), \quad (7)$$

$$= \text{NSE}\left(\text{SWE-REF}, \frac{\text{SWE-DL}}{\max(\text{SWE-DL})} \times \max(\text{SWE-REF})\right) \quad (8)$$

317 where  $\max(\text{SWE-REF})$  represents the historical maximum SWE from the reference dataset,  
 318 and  $\max(\text{SWE-DL})$  denotes the historical maximum SWE from the DL models. Equa-  
 319 tions 7 and 8 are equivalent since the NSE value is unaffected when the predictions and  
 320 observations are multiplied or divided by the same constant. As opposed to the NSE of

absolute SWE, the NSE of SWE fraction emphasizes the temporal features and de-emphasizes errors in magnitude.

Model performance is further quantified using root mean squared error (RMSE) and mean absolute error (MAE),

$$\text{RMSE}(O_t, P_t) = \sqrt{\frac{\sum(O_t - P_t)^2}{n_{\text{samples}}}}, \quad (9)$$

$$\text{MAE}(O_t, P_t) = \frac{1}{n_{\text{samples}}} \sum |O_t - P_t|. \quad (10)$$

where  $n_{\text{samples}}$  is the number of evaluated samples. RMSE and MAE are in the range  $[0, +\infty)$  with lower values indicating a closer match, and a score of 0 indicating a perfect match between the model and observations.

## 2.7 Feature Permutation

Although DL models generate accurate predictions, they are frequently referred to as ‘black box’ models since it is often unclear why and how the model produces its results. Recent advances in explainable AI (XAI) have enabled better interpretation of DL model results, especially in Earth system modeling (McGovern et al., 2019; Gagne II et al., 2019; Barnes et al., 2020; Toms et al., 2020). Such techniques are further useful for building credibility in DL models by demonstrating that they are mimicking physical understanding and principles.

Permutation-based XAI methods are commonly used to quantify the relative importance of input variables in the DL models (Breiman, 1996). The permutation method evaluates the DL model by first obtaining a baseline performance score. Then each feature is permuted to generate a shuffled dataset, and a new performance score is calculated. The change in the performance score represents the importance of a given feature. A greater decrease in model skill corresponds to higher feature importance. This approach follows previous work addressing model interpretation (Gagne II et al., 2019). However, care should be taken in the interpretation of these results, as the quantified performance is potentially confounded by correlation among input features. For example, a model that uses both mean and maximum daily temperature as input may see minimal performance loss from the removal of either of these features while the removal of both would be significant. Efforts to address correlation issues include the use of multi-pass permutation, as discussed in a review by McGovern et al. (2019).

In this study, we permute both the training and the testing set and train a reduced model. By permuting the training set and retraining the model, the permuted variable is blocked and the reduced model only receives the information from the remaining non-permuted variables. The importance of the permuted variable will be quantified by examining the ratio of the new NSE value against the baseline score. The permutation is performed separately for dynamic inputs and static variables. For dynamic inputs, the time series from each grid point is used for re-sampling so that the statistical properties of these variables are preserved (i.e., only the time steps are shuffled). For static features, the permutation is performed among all stations.

## 2.8 Switching the Model Target for Spatial Extrapolation

DL models generally yield accurate predictions when interpolating between unseen samples in the training set range, but can struggle when extrapolating beyond this range. With that said, Balestriero et al. (2021) showed that in high-dimensional data with the training range defined by the convex hull of the training set (i.e., the minimal convex polygon that encompasses all the training points), samples almost always fall in the extrapolation regime. This is particularly true for time series problems, where the dimension is the product of input time window size and a number of input features. For the problem investigated here, extrapolation is most obvious when the SNOTEL-trained model

367 is applied to the whole Rocky Mountains, since these stations are largely found only in  
 368 high-elevation regions. To mitigate some of the effects of extrapolation, an alternate model  
 369 target is considered in this work.

370 To alleviate problems with extrapolation, a second set of DL models are trained  
 371 with SWE fraction as a target, which is defined as the SWE normalized by the histor-  
 372 ical maximum SWE at each station. In this case, the model output is generally less than  
 373 1, though exceedance of maximum historical SWE is allowed and would produce values  
 374 greater than 1. Consequently, for the SWE fraction, model normalization is not needed  
 375 (i.e., equation 4). When extrapolating to a low-elevation area, the DL estimation is com-  
 376 pared against the reference dataset. The absolute SWE can be recovered by multiply-  
 377 ing the model result by the historical maximum SWE. In this case, the NSE of SWE frac-  
 378 tion (equation 8) can be written as

$$\text{NSE}_{\text{fraction}} = \text{NSE}(\text{SWE-REF}, \text{SWE-DL-FRAC} \times \max(\text{SWE-REF})) \quad (11)$$

$$= \text{NSE}\left(\frac{\text{SWE-REF}}{\max \text{SWE-REF}}, \text{SWE-DL-FRAC}\right), \quad (12)$$

379 where SWE-DL-FRAC denotes the DL model predicted SWE fraction.

### 380 3 Model Performance at SNOTEL stations

#### 381 3.1 Computational Performance

382 The training time for each DL model on a single RTX 2080TI GPU is 5 hours for  
 383 the LSTM model, 10 hours for the TCNN model, and 26 hours for the Attention model.  
 384 Although the training time varies among different DL models, all DL models only need  
 385 to be trained once, and inference time is much shorter. Inference time at SNOTEL sta-  
 386 tions is on the order of a few minutes. For our application over the Rocky Mountains,  
 387 it takes approximately 35 minutes to generate a 10-year prediction of SWE on the 168  
 388  $\times$  108 grid cells covering the Rocky Mountains with parallel execution on a single RTX  
 389 2080TI GPU for either the LSTM and TCNN. The Attention model takes longer than  
 390 the other DL models to generate a prediction – approximately 2.5 hours without par-  
 391 allel execution – and is limited by the GPU memory. Faster performance is anticipated  
 392 using GPUs with larger memory. Given the much faster inference time, the training time  
 393 is not used for model selection or intercomparison.

#### 394 3.2 Temporal Prediction

395 Following DL model training, DL model performance is evaluated over the test-  
 396 ing period (2008-10-01 to 2018-09-30) at all SNOTEL stations. Since summertime SWE  
 397 is zero at most SNOTEL stations, daily information for both the entire testing period  
 398 and only those days in the testing period when observed SWE is nonzero are examined  
 399 separately. As discussed in section 2.1, the mean from a 10-member ensemble SWE pre-  
 400 diction for each DL model and SNOTEL station is used for analysis. Table 1 shows the  
 401 median NSE, MAE and MSE across all SNOTEL stations. Among the DL models, the  
 402 LSTM has the highest median NSE value, followed by the TCNN and then the Atten-  
 403 tion model. The distribution of NSE values is further shown in Figure 2. The LSTM cu-  
 404 mulative distribution function (CDF) lies above the TCNN and Attention CDF, indi-  
 405 cating that the LSTM produces more station SWE predictions with higher NSE values,  
 406 compared with the TCNN and Attention models. When only comparing the TCNN and  
 407 Attention models, the TCNN has a slightly higher median performance, although the  
 408 Attention model shows better overall performance. An example of SWE prediction for  
 409 a single SNOTEL station is given in Figure S5.

410 Prediction accuracy is also computed for the UA and the UCLA dataset over the  
 411 same testing period using the nearest grid point to the SNOTEL station (further dis-

**Table 1.** Tabulated model performance for prediction of SWE at SNOTEL stations. The top table shows performance scores on dates when observed SWE is greater than zero, while the bottom table shows the whole evaluation period (from 2008 to 2018). The best scores for each metric are shown in bold font.

Nonzero SWE	Median NSE	Median MAE (mm)	Median RMSE (mm)
LSTM	<b>0.823</b>	<b>42.97</b>	<b>63.14</b>
TCNN	0.792	52.58	73.14
Attention	0.779	52.03	72.06
UA	0.755	49.77	73.02
UCLA	0.482	77.31	104.51
SNOW-17	0.488	80.34	102.39

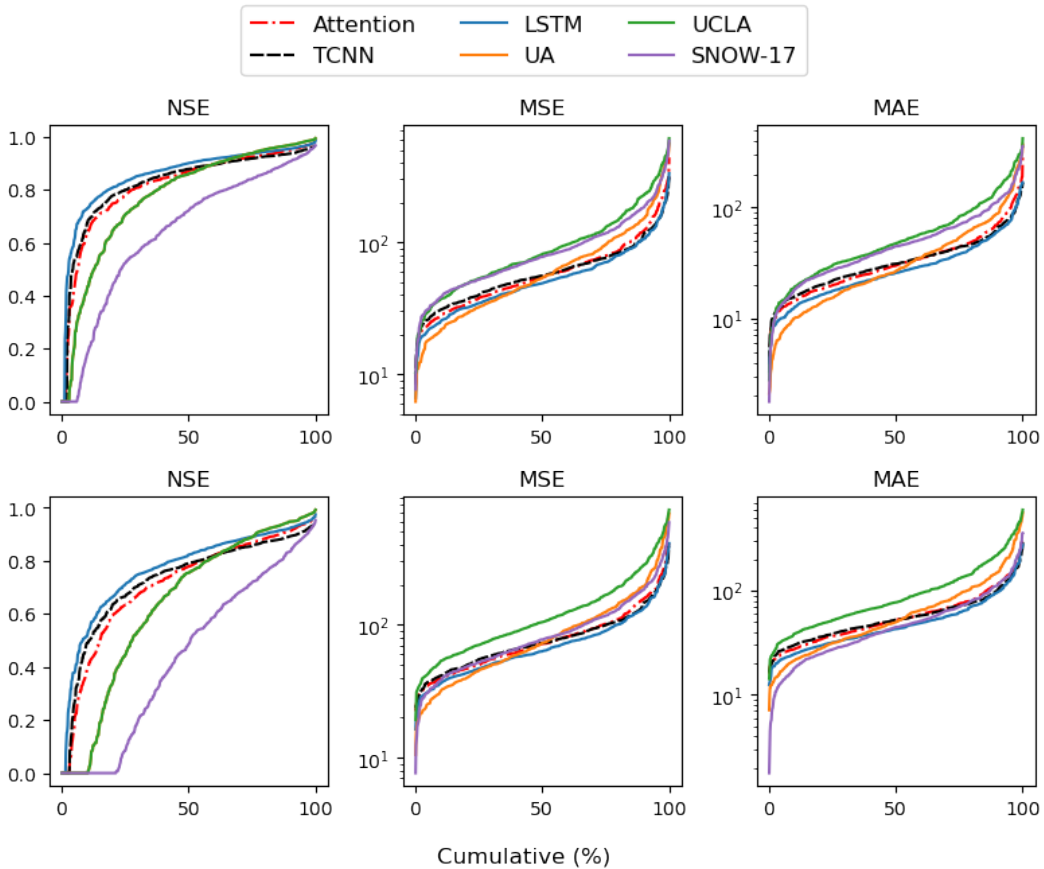
  

Whole period	Median NSE	Median MAE (mm)	Median RMSE (mm)
LSTM	<b>0.901</b>	<b>25.76</b>	<b>49.03</b>
TCNN	0.879	31.07	55.76
Attention	0.871	29.93	54.08
UA	0.861	26.69	53.61
UCLA	0.708	47.16	81.19
SNOW-17	0.722	44.69	77.45

cussion of the potential impact of this choice on accuracy is provided in section 5). The median NSE values over the whole testing period are 0.861 and 0.482 for the UA and UCLA dataset, respectively. For those days when observed SWE is nonzero, the NSE score is 0.755 for the UA dataset and 0.708 for the UCLA dataset. Under this metric, all DL models achieve better results than these two datasets. Moreover, when comparing the distribution of NSE values in Figure 2, we see that the DL models produce more stations with higher NSE values. As for MAE and MSE metrics, the UA dataset achieves a lower median MAE than the TCNN and Attention for both the whole testing period and the nonzero-SWE period. Examining Figure 2, the UA dataset also attains the lowest MSE and MAE across 20% to 30% of SNOTEL stations.

Finally, prediction accuracy from the DL models is compared with the SNOW-17 model. Under all three metrics, all DL models attain higher NSE scores and lower MAE and MSE values than SNOW-17. Since we used the same training period to calibrate the SNOW-17 model, missing values may affect model parameters at some locations. In fact, the median NSE score for the SNOW-17 model increases to 0.778 when only those stations with less than one year of missing values are taken into consideration. Nonetheless, this score is still lower than the DL models. Possible reasons are discussed further in Section 5.

To better understand the drivers of model performance, we examine relationships between NSE, elevation, and maximum SWE. Figure 3 shows the NSE distribution with respect to elevation. In general, all DL models and process-based model/datasets perform better at higher elevation. For the DL models, performance improvements are also positively correlated with maximum SWE (as shown in Figure 4). This relationship is not obvious among the process-based models, and seems to only hold for maximum SWE below 1500mm (1000mm for UCLA). However, sharp variations in performance can be partially attributed to low sample size for high maximum SWE. This result appears to be a common theme in our study: at higher elevations and in regions of deeper maximum SWE, snowpack is easier to predict. We hypothesize that this is because there is less uncertainty in rain-snow partitioning at higher elevation, and because the processes



**Figure 2.** Cumulative distribution functions across three model performance metrics for predicting SWE across SNOTEL stations in the western US. NSE values are truncated at 0. The upper row shows model performance when only those SWE observations larger than zero are used. The lower row shows model performance for all zero and nonzero SWE observations. Higher scores in the first column, and lower scores in the second and third columns, are indicative of higher performance.

that occur at the interface between land surface and snowpack are strongly nonlinear, but become less important when a deep snowpack is present.

To summarize, for western US SNOTEL stations, DL models can generally produce comparable results with the selected process-based model and datasets, and share a similar relationship between performance and elevation. Among all models, the LSTM model provides the most accurate predictions across the three DL models assessed. Although the three DL models exhibit differences in performance, the spatial distribution of their performance tends to be similar – that is, stations with lower (higher) NSE values in one model tend to have lower (higher) NSE values in other models. Across DL models, the Pearson correlation of NSE is 0.856 and 0.660 for TCNN and Attention versus LSTM (Figure S6). As shown in Figure 5, all DL models exhibit relatively poor performance (i.e., negative NSE values) in Western Washington, Northern Nevada, Southern and Northwestern Oregon, and Northern Montana. In general, these stations tend to have a lower maximum SWE than other stations, which is consistent with our earlier attribution of model performance (Figure 4). These also tend to be regions where the UCLA product performs poorest, while the SNOW-17 and UA datasets are more vari-

able. Importantly, these results should not be taken as being indicative of the UA product being higher quality than the UCLA product. While the UA dataset assimilates SNOTEL observations, the UCLA dataset relies almost exclusively on remote sensing, as outlined in Section 2.4. Consequently, the relatively strong performance of the UA dataset is unsurprising when evaluated against SNOTEL observations. A more thorough comparison between the UA and UCLA datasets (and, more generally, observational spread) would require an independent data source (e.g., the Airborne Snow Observatory), which lies beyond the scope of this study.

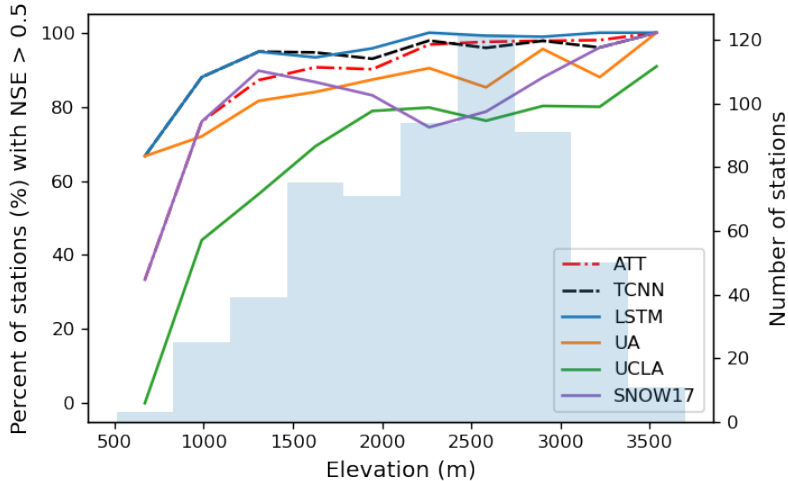


**Figure 3.** NSE value distribution with respect to elevation. The left y-axis denotes the fraction of stations with NSE values higher than 0.5 for each elevation bin. The right y-axis shows the number of SNOTEL stations in each elevation bin.

### 3.3 Spatial Cross-Validation

The ability of the model to transfer its understanding of physical processes from one region to another is now assessed, as we build towards the development of a gridded SWE product. Hereafter, our study will focus exclusively on the LSTM because of its superior performance compared with other DL models and its strong correlation with those models across stations. Among 581 SNOTEL stations, 530 are located inside the mountain range boundaries in Serreze et al. (1999) and M. He et al. (2011b). The two spatial splittings employed here are described in section 2.3, and are referred to as ‘mountain cross-validation’ for splitting (2a) and ‘8-fold cross-validation’ for splitting (2b). The ‘time-split’ experiment which was analyzed in section 3.2 is used as a reference. Results from this experiment are given in Figure 6 and Table 2. Overall, the ‘time-split’ LSTM yields the best prediction accuracy, with a median NSE score of 0.899, followed by the ‘8-fold cross-validation’ and ‘mountain cross-validation’ LSTMs, with the NSE scores of 0.888 and 0.844, respectively. Compared with our full model that trained with 581 SNOTEL stations, we do see a tendency of better performance with more training stations. This suggests the benefit of a large and diverse training set, which was also argued in K. Fang et al. (2022).

Grouped by mountain ranges, Idaho/Western Montana and northwestern Wyoming areas exhibit stronger performance, while the Cascades produces the lowest median NSE score, which is especially pronounced for the ‘mountain cross-validation.’ This suggests there are unique snow dynamics in the Cascades that other mountain ranges appear unable to capture. In addition, predictability is limited in Arizona/New Mexico (AZ/NW),

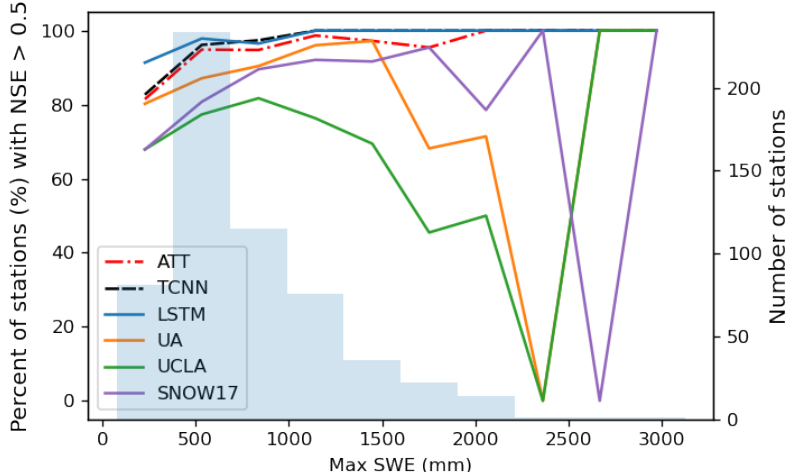


**Figure 4.** NSE value distribution with respect to maximum SWE measurement. The left y-axis denotes the fraction of stations with NSE values higher than 0.5 for each SWE bin. The right y-axis shows the number of SNOTEL stations in each SWE bin.

**Table 2.** Median NSE values for SNOTEL stations in major mountain ranges. Northwestern Wyoming is abbreviated to NW Wyoming and Arizona/New Mexico to AZ/NW. Numbers in parenthesis denote the number of SNOTEL stations in each mountain range.

	Cascades (78)	Sierra Nevada (24)	Blue Mountains (26)	Idaho/Western Montana (95)	
Time-split	0.853	0.878	0.862	0.923	
Cross-validation	0.812	0.845	0.879	0.914	
Mountain-based	0.741	0.846	0.852	0.894	
	NW Wyoming (110)	Utah (74)	Colorado (109)	AZ/NW (19)	Overall (530)
Time-split	0.921	0.911	0.907	0.856	0.899
Cross-validation	0.901	0.891	0.892	0.792	0.888
Mountain-based	0.877	0.867	0.833	0.758	0.844

the southernmost of our selected mountain ranges. These results are not surprising given the distinct topographical features of these regions: the elevation is much lower in the Cascades compared with other mountain ranges (shown in Figure 6), while the AZ/NW mountains experience relatively warm temperatures and lower maximum SWE. Indeed, when the AZ/NW mountains are used for testing, elevation and latitude are completely out of the training range. This is an obvious example of model extrapolation, the likely explanation for this range's relatively poor performance, and suggests a need for more observational data from a variety of snow regimes. Nonetheless, the DL model performance in this test exceeds NSE scores derived from SNOW-17 and the UCLA product.

### 3.4 Permutation-Based Analysis

The variables that are most important for the LSTM model are now studied using a permutation-based analysis. As described in section 2.7, a new set of LSTM models are trained and tested with the shuffled datasets. The importance of each input variable is quantified by comparing the ratio of the permuted LSTM model whole period NSE prediction to the LSTM model baseline NSE prediction, which is trained and tested with the non-permuted dataset. The permuted LSTM models are also trained 10 times to build an ensemble of predictions. To quantify model uncertainty, we use bootstrap sampling

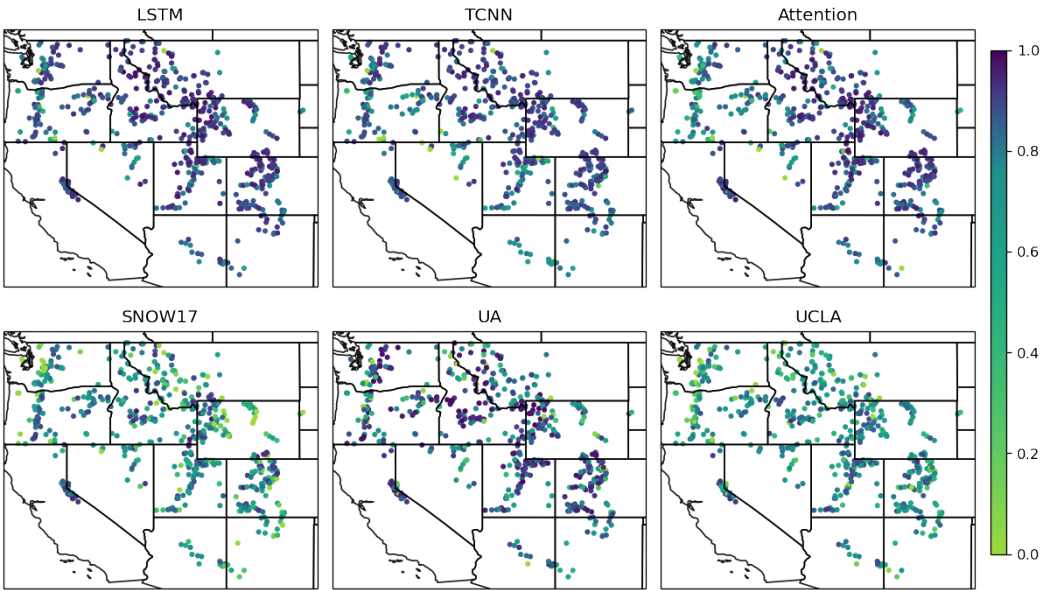


**Figure 5.** SWE prediction performance from the DL models, the SNOW-17 model, and the UA and UCLA datasets. Dots represent individual SNOTEL stations, with the color of the dot representing the NSE value (truncated at 0).

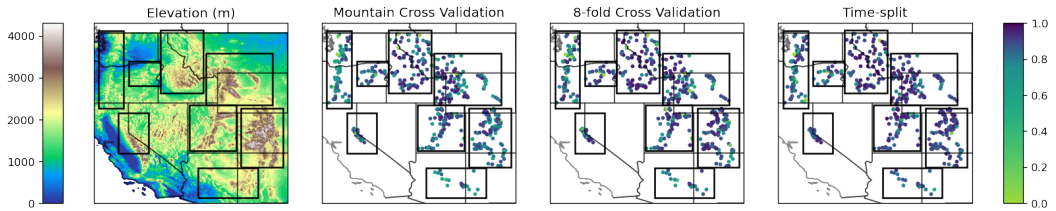


**Figure 6.** SWE prediction performance from the LSTM with spatial cross-validation. Elevation is shown on the left as a reference. Dots represent individual SNOTEL stations, with the color of the dot representing the NSE value (truncated at 0). Mountain-based cross-validation is depicted on the left, random 8-fold cross-validation in the middle, and the time-split result is shown on the right for reference. Black boxes represent the mountain region boundaries.

to provide results with a 90% confidence interval. In Figure 7, the green bars represent the performance decline for each static variable, the blue bars represent the performance decline from individual meteorological variables, and the orange bar represents the combined effect of all static variables.

The input variable with the most influence on model performance was precipitation, followed by elevation, while the rest of the input variables had comparable influence. This result agrees with the intuition that precipitation provides water mass to build snowpack, and precipitation type is determined by temperature (and humidity), which is shaped by elevation via the lapse rate (Jennings et al., 2018). Although this result seems like common sense and may be affected by the collinearity between input variables, it helps build trust in the LSTM model and provides evidence that it follows basic physical principles. The combined effect of static features is also demonstrated to be critical, as the LSTM model accuracy would drop approximately 7% without their inclusion, which is more than half the influence of precipitation. Clearly, these features are use-

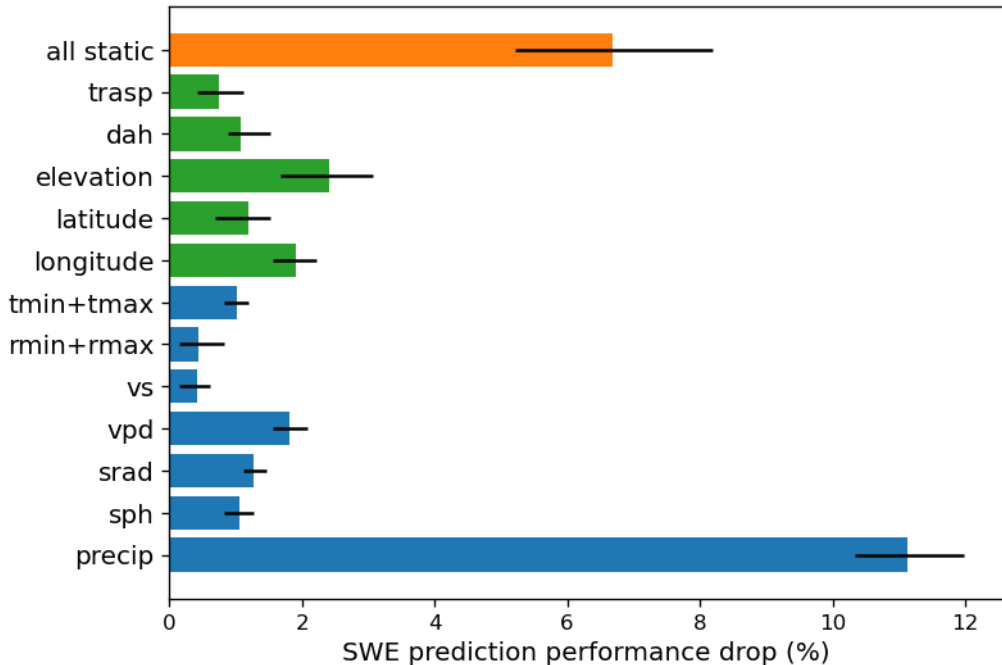


**Figure 7.** SWE prediction performance drop (%) quantified using the NSE values among the permuted estimates. Error bars represent the 90% confidence interval from bootstrap sampling. Precipitation is abbreviated to ‘precip’, ‘sph’ stands for specific humidity, ‘srad’ for solar radiation, ‘vpd’ for vapor deficit, and ‘vs’ for wind speed. ‘Tmin’, ‘tmax’, ‘rmin’, and ‘rmax’ refer to minimum and maximum temperature and relative humidity.

ful for modulating snowpack dynamics at each SNOTEL station and in out-of-sample locations during extrapolation. The utility of static variables was also reported in Kratzert et al. (2019b), where LSTM models were used to predict streamflow.

Among all static variables, there are three categories: location (latitude and longitude), aspect and slope (DAH and TRASP), and elevation. We combined each static variable into these categories during the permutation process to compare their relative importance. Relative to the baseline LSTM model with a median NSE of 0.901, the LSTM model that did not include location information had the highest median NSE score (0.878), followed by aspect and slope (0.874), and elevation (0.870). Despite being rather modest drops, this result again emphasizes that elevation information is the most important in SWE prediction since it can determine the temperature and rain-snow partitioning of precipitation. Although the local temperature is also affected by latitude through differences in solar loading, the LSTM model benefited more from information related to aspect and slope, which have more localized effects on temperature.

Because many of these variables are correlated, care should be taken in attributing the relative importance of variables other than precipitation under the permutation test. This is especially true for temperature, since vapor deficit is a function of temperature and relative humidity and consequently, temperature can be inferred from vapor deficit and relative humidity even if we permute temperature. To better compare their relative influence on SWE predictability, several reduced-order LSTM models are trained. In each reduced-order model, precipitation and one of the other meteorological variables are used, and the remaining variables are permuted. The baseline for comparison was an LSTM model with only precipitation and the reference was a model with the full set

**Table 3.** First quantile, median and third quantile whole period NSE from several reduced-order LSTMs for predicting total SWE. Precipitation is abbreviated to Precip.

	First Quantile NSE	Median NSE	Third Quantile NSE
Precipitation Only	0.149	0.380	0.576
Precip+Wind Speed	0.432	0.620	0.740
Precip+Specific Humidity	0.686	0.826	0.896
Precip+Solar Radiation	0.709	0.836	0.905
Precip+Vapor Deficit	0.740	0.843	0.894
Precip+Temperature	0.793	0.874	0.924
Precip+Temperature+Relative Humidity	0.784	0.875	0.919
Precip+Temperature+Vapor Deficit	0.818	0.881	0.927
Precip+Temperature+Specific Humidity	0.799	0.882	0.927
Precip+Temperature+Wind Speed	0.803	0.884	0.926
Precip+Temperature+Solar Radiation	0.813	0.886	0.931
Full Model	0.831	0.901	0.938

of meteorological variables. The model using precipitation plus relative humidity was not included in this analysis because it did not converge to a reasonably performant model. As shown in Table 3, among the reduced-order models, precipitation and wind speed give the lowest NSE value, although even this combination does improve skill tremendously compared with the baseline model. The median NSE scores across the rest of the reduced-order models are all above 0.8, and the combination of temperature and precipitation produces the closest performance to the reference model. This indicates that vapor pressure deficit, solar radiation, and specific humidity contain influential information for SWE prediction, while temperature is the most critical variable for model skill besides precipitation.

To determine the best third variable in the model, five additional models were trained: each model consists of precipitation, temperature, and one other variable. The results are shown in Table 3. The model with precipitation, temperature and relative humidity attains the lowest NSE value and is very close to the model with only precipitation and temperature, which is consistent with previously observed anomalous low performance with precipitation and relative humidity. The inclusion of vapor deficit, specific humidity and wind speed all increase the model performance and yield similar NSE scores, probably because these variables cannot be inferred from precipitation and temperature. The model with precipitation, temperature and solar radiation obtained the highest median NSE value of 0.886, or 98% of the full model performance. Clearly, with far fewer input variables, the model with precipitation, temperature and solar radiation was capable of capturing the temporal features necessary for SWE prediction. This again highlights the important roles that these three variables have in affecting the water cycle (S. Duan et al., 2020). Additionally, this result suggests that good estimates of snowpack can be obtained from datasets providing these quantities in high quality, such as CAMELS (Addor et al., 2017).

One additional model was trained to capture some of the diurnal cycle of temperature through inclusion of both minimum and maximum temperature (as opposed to daily average temperature). The improvement in median NSE was only 0.002, suggesting minimal value to the inclusion of both variables (more information in Table S1 and Text S2).

## 571 4 Spatial Extrapolation of DL Models to the Rocky Mountains

572 Our earlier analysis indicates that DL models are capable of predicting daily SWE  
 573 at individual SNOTEL stations and can even achieve satisfactory performance when ex-  
 574 trapolating to stations out of the training set. A gridded SWE product similar to the  
 575 UA and UCLA datasets is now developed by applying these models out-of-sample across  
 576 the Rocky Mountains at 4km grid spacing (Figure 8). It is shown that the resulting prod-  
 577 uct is reasonable, even when there are out-of-sample differences in the statistical prop-  
 578 erties of the DL models' input and output variables. The use of these models outside of  
 579 their training range is a common problem referred to within the machine learning com-  
 580 munity as concept drift or extrapolation (Tsymbal, 2004). In this case, extrapolation is  
 581 expected to be common since, in addition to other differences, many grid points have el-  
 582 evations lower or higher than the lowest or highest SNOTEL station (this was also hy-  
 583 pothesized to have impacted model performance over the Cascades and New Mexico in  
 584 Table 2).

585 The 4km grid used in this application is inherited from the gridMET forcing data  
 586 (section 2.2). A similar approach could also be used to produce an even higher resolu-  
 587 tion product (e.g., one matching the 800m Parameter-elevation Regressions on Indepen-  
 588 dent Slopes Model (PRISM) product). The simulation period is 2008-10-01 to 2018-09-  
 589 30, the same as the SNOTEL testing set. For better comparison across different spatial  
 590 resolutions, the gridMET data is also regridded to the UA and UCLA grid points us-  
 591 ing the nearest neighbor method. When applied over the Rocky Mountains, the gridMET  
 592 forcing variables are normalized with the mean and standard deviation from the train-  
 593 ing SNOTEL stations (equation 4). The DL model SWE prediction is then transformed  
 594 back to its original units with the same equation. The top row in Figure 9 and 10 shows  
 595 the NSE values obtained from the DL-generated dataset (10 ensemble member mean)  
 596 when using the UA dataset and UCLA dataset as reference, respectively, following equa-  
 597 tion 6.

598 The DL model estimates largely agree with the process-based estimates in high-  
 599 elevation areas, while performance is relatively poor in low-elevation areas. Given that  
 600 much of the domain is covered by low-elevation areas, it is useful to investigate the rea-  
 601 sons for this poor performance and develop models which can mitigate these errors. One  
 602 obvious driver of poor performance is the sensitivity of NSE to differences that are rel-  
 603 atively small in absolute magnitude, when maximum SWE is already small. This is il-  
 604 lustrated by comparing the UA and UCLA datasets (middle and right figures in Figure  
 605 8). Negative NSE values abound in low-elevation areas (e.g., the northwestern Rockies,  
 606 36°N-37°N and 109°W-108°W), suggesting significant disagreement between these two  
 607 products in this region. This difference also appears in Figure 3, where both DL mod-  
 608 els and the UA and UCLA datasets exhibit poor performance at lower elevations and  
 609 when SWE amounts are low – indeed, the ground truth in these regions is poorly con-  
 610 strained given a dearth of relevant measurements. The discrepancy between UA and UCLA  
 611 in this region is likely exacerbated by the employ of different algorithms and data sources:  
 612 UA is not informed by remote sensing estimates, but is informed by SNOTEL stations,  
 613 while the opposite is true for the UCLA product. These factors make it difficult to quan-  
 614 tify how much error may be attributed to the out-of-sample application of the DL model.

615 To better understand the reasons for poor performance in low-elevation areas, er-  
 616 rors in this region are decomposed into errors in magnitude estimation (i.e., too little  
 617 or too much SWE) and errors in temporal dependency (i.e., too slow/rapid accumula-  
 618 tion/melt). To mitigate issues related to magnitude estimation, model performance is  
 619 assessed using the fraction of maximum SWE (i.e., SWE/ max SWE), where the max-  
 620 imum is with respect to the historical/training period. That is, the NSE from snow frac-  
 621 tion is calculated via equation 7. By using the SWE fraction, differences in SWE mag-  
 622 nitude between the reference datasets and DL model are mitigated and so the evalua-  
 623 tion emphasizes the temporal character of the SWE (e.g., the timing of accumulation

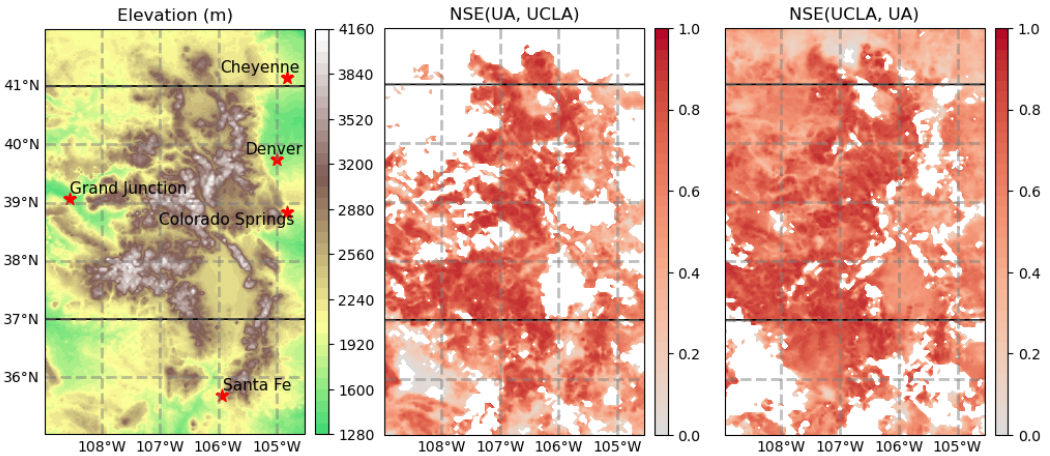


**Figure 8.** Elevation (left) along with NSE scores between reference datasets with UA as reference (middle) and UCLA as reference (right) over the Rocky mountain area.

and melt). The middle row in Figure 9 and 10 shows the assessment with SWE fraction. Under this metric, the DL model appears significantly better when evaluated against the UA dataset in Figure 9, with higher NSE values almost everywhere and a larger portion of positive NSEs. This difference indicates that while the DL models can capture the temporal dependence of SWE, magnitude biases can be relatively large over low-elevation areas. However, when the UCLA dataset is used as a reference, the fractional SWE metric does not always lead to improvements in the performance of the DL models (Figure 10): in fact, only the TCNN model produces more grid points with positive NSE values, indicating some temporal feature mismatch between the LSTM and Attention models and the UCLA dataset that cannot be mitigated under this metric. Despite the overall decrease in the fraction of positive NSE scores for the LSTM and Attention models, there are indeed improvements over the mountain range to the northeast of Santa Fe (36N-37N, 106W-105W). This pattern of improvement is consistent across all the DL models and independent of the reference dataset, as similar patterns are also observed in Figure 9.

Given the improvement in model performance when using SWE fraction, a new set of DL models is trained on SNOTEL data to predict SWE fraction (section 2.8), rather than the SWE itself (with predictions hereafter referred to as SWE-DL-FRAC). NSE values are then computed using equation 12. It should be noted that equation 8 and 12 are not equivalent and they represent two different comparisons. Equation 8 uses the original DL models, which predicts SWE magnitude normalized by the historical maximum prediction; whereas the maximum SWE in equation 12 is from reference datasets and the DL models are predicting SWE fractions. The bottom row in Figure 9 and 10 show the NSE results when predicting SWE fraction directly from the DL models. When compared to the original DL models which predict SWE magnitude, the DL models trained to predict SWE fraction exhibits a clear and significant improvement almost everywhere in the domain, but particularly in low-elevation regions. This result shows that normalization by maximum SWE is effective for all the DL models with both reference datasets. Among all the DL models, the LSTM-based model again provides the best overall SWE prediction, determined by the largest fraction of positive NSE values. Of course, to transform the fraction of maximum SWE back to an absolute SWE value, the historical maximum SWE is needed within each grid cell. Since SNOTEL observations are unevenly distributed throughout the Rocky Mountains, we must rely on an alternative estimate of maximum SWE at each grid point; in this case, we use the historical maximum SWE

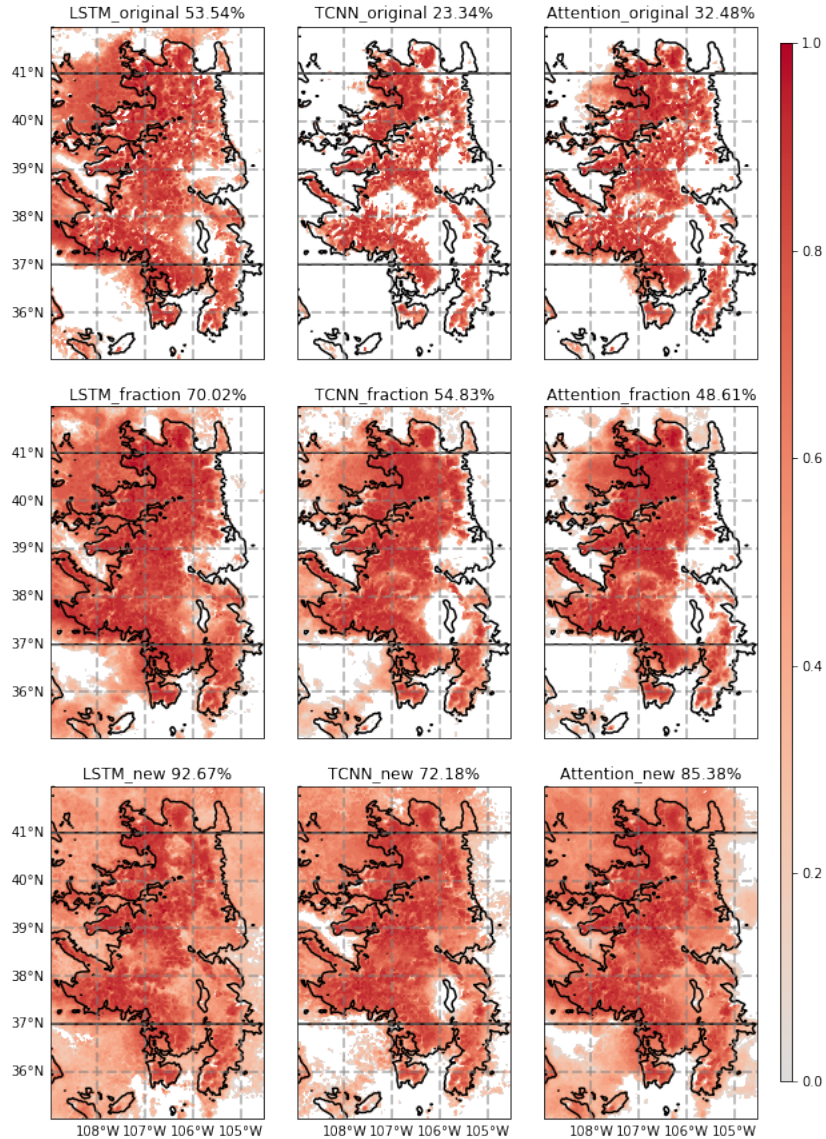


**Figure 9.** NSE values for DL model extrapolation estimates over the Rocky Mountains with the UA dataset as reference. The top row shows the NSE score of the original DL model SWE predictions. The middle row is the SWE fraction evaluation from the original models, computed via equation (7). The bottom row represents the new set of DL models that predict SWE fraction, computed via equation (12). NSE values below 0 are masked in all figure subpanels. The black line is the 2300-meter contour. The percentage value given in the title is the fraction of grid points with positive NSE values.

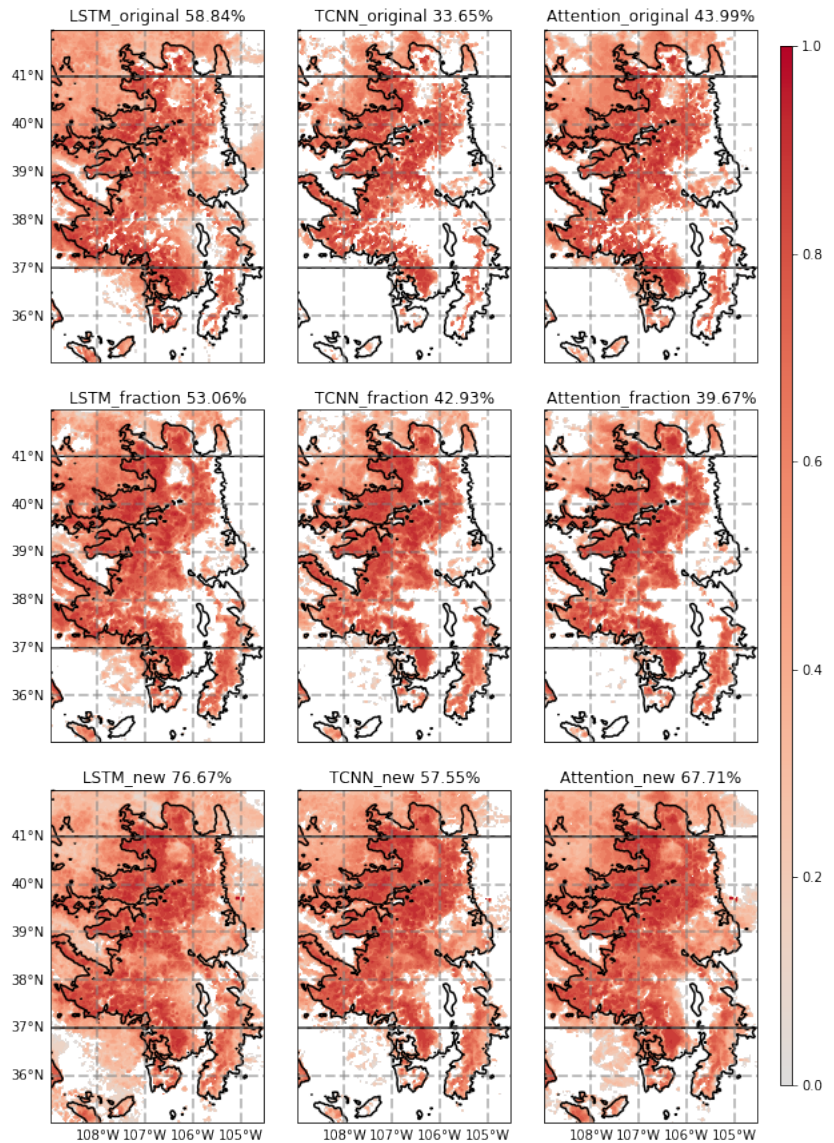


**Figure 10.** Same as Figure 9, but with the UCLA dataset as reference.

values from the reference dataset, either the UA or UCLA dataset, at each grid point over the training period to estimate maximum SWE. An example of annual maximum SWE prediction from this new LSTM model is shown in Figure S7.

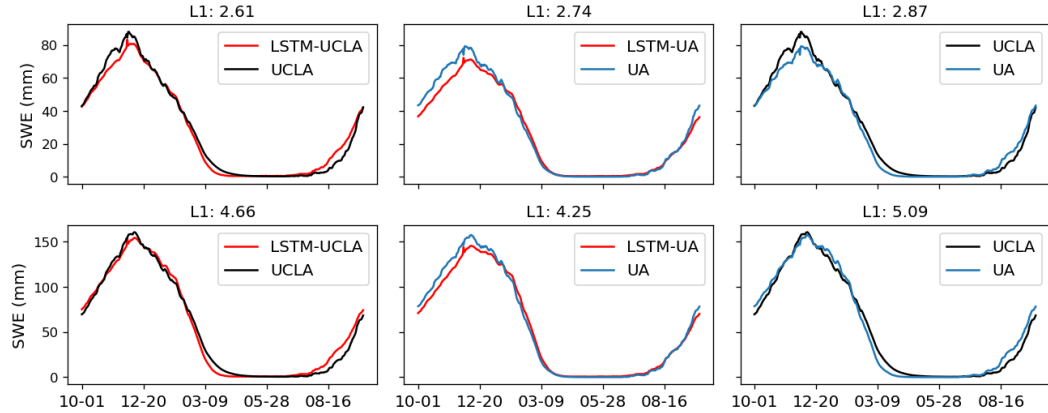


**Figure 11.** Area-averaged SWE climatology over the Rocky Mountain area. The first row depicts results from the whole region, while the second row depicts only the area above 2300m. ‘UCLA’ and ‘UA’ stand for the results from the reference datasets. SWE fraction from LSTM is transformed back to SWE depth and the results are denoted with the corresponding reference datasets. The title for each subfigure denotes the L1 norm between the two climatology estimations.

LSTM performance is further analyzed by examining the annual SWE climatology over the Rocky mountains. The SWE estimation in millimeters, which is derived from the DL-generated SWE fraction and reference datasets as in equation 12, is averaged over the Rocky Mountain area and compared against the reference dataset. In Figure 11, ‘LSTM-UCLA’ is derived from the LSTM estimation and historical maximum SWE from the UCLA dataset, whereas ‘LSTM-UA’ uses the UA dataset to derive the historical maximum SWE. In general, the LSTM model matches the reference dataset, with correlation coefficients exceeding 0.99. The LSTM model does, however, have a tendency to underestimate the snowpack peaks, but this bias decreases in higher-elevation areas. The magnitude difference between these two reference datasets is also worth noting. Averaged over the whole area, a higher peak SWE is observed in the UCLA dataset, which again tends to diminish with elevation. This suggests that both process-based and DL models have significant uncertainties in their SWE estimations over the low-elevation areas. Comparing the L1 norm between climatology estimations (the subtitles in Figure 11), the LSTM L1 norm is smaller than those for the reference datasets, i.e.,  $L1(UCLA, UA)$  is the largest for both whole-area and high-elevation climatology estimations. This suggests the LSTM model is always in the uncertainty range of the selected process-based datasets, which provides evidence of its credibility.

In addition to differences in peak SWE, these models/datasets yield different accumulation and melt dates. Both the UA dataset and the LSTM model exhibit earlier accumulation (melt) dates when the SWE starts increasing (hits zero) in comparison to the UCLA dataset. Unlike the magnitude bias, this difference persists as elevation increases. We are not able to determine which model/dataset generates the more precise melt date. A further evaluation is needed to draw such conclusions, which is out of our scope here.

686 **5 Discussion**

687 One question that arises in this study relates to the importance of horizontal res-  
 688 olution for the accuracy of the SWE prediction. Obviously, higher resolution alone should  
 689 not be conflated with higher performance – but in mountainous regions, where topog-  
 690 raphy and solar insolation can vary rapidly over short distances, the resolution is impor-  
 691 tant to properly capture SWE daily-to-seasonal cycles. However, significant uncertain-  
 692 ties in snow products persist over short distances, which are exemplified by a relative per-  
 693 formance at SNOTEL station locations. In table 1, the UCLA product was first regrid-  
 694 ded to the 4km UA grid, then interpolated to SNOTEL station locations for compar-  
 695 ison, yielding a median NSE of 0.708. However, directly regressing the UCLA product  
 696 to the SNOTEL station location, which one might expect would be far more accurate  
 697 because of the finer grid spacing of the UCLA product, yields an even lower median NSE  
 698 of 0.641 when assessed over the whole period. While this difference is likely to be pri-  
 699 marily driven by observational uncertainty in SWE, we postulate that there may be an-  
 700 other factor in play: specifically, given the significant differences in snow dynamics over  
 701 relatively short spatial distances, it may be the case that accumulating SWE over a coarse  
 702 grid cell may mute sharp variations in the spatial character of SWE and so could match  
 703 more closely to the SNOTEL station. This is also corroborated by the spatial variabil-  
 704 ity of UCLA SWE estimations within the UA grid boxes, as illustrated in Figure S8.

705 Because of the relatively fine scale of mountainous features, it is also the case that  
 706 high-resolution static inputs do not necessarily yield better performance. The impact of  
 707 static feature resolution is investigated with the PRISM 800-meter topographic data (Daly  
 708 et al., 2008). This data was used to derive elevation, TRASP and DAH for the LSTM  
 709 model, and compared with TRASP and DAH inputs from 30-m USGS DEM data. At  
 710 800-m spatial resolution, the derived slope and aspect are unlikely to represent the slope  
 711 and aspect at the SNOTEL station, and consequently may be invalid for use in DL mod-  
 712 els of SWE. However, the performance of the LSTM model with coarse TRASP and DAH  
 713 actually increases slightly: from a median NSE of 0.901 (30-m DEM) to 0.911 (800-m  
 714 DEM). This change is nonetheless significant under Mood’s median test (*p*-value equals  
 715 0.019). This increase in performance suggests that, at least for these features, DL mod-  
 716 els do not explicitly require precise topographical features for SWE prediction. This re-  
 717 sult is again likely because the significant spatial heterogeneity of mountainous regions  
 718 at finer spatial scale makes it difficult to extract a clear signal from the noise.

719 In this study, nearest neighbor interpolation has been applied for both in-situ and  
 720 gridded product evaluation. However, it could be that this interpolation method is re-  
 721 sponsible for degrading model performance. This interpolation error is now investigated  
 722 when the LSTM model is applied to develop the gridded Rocky Mountain SWE prod-  
 723 uct. 105 SNOTEL stations inside the Rocky Mountains are selected, and four predic-  
 724 tions with different interpolation processes are assessed: in-situ LSTM predictions ('LSTM-  
 725 in-situ'), reference datasets (either 'UA' or 'UCLA'), SWE fraction from LSTM ('LSTM-  
 726 extra-FRAC') and SWE depth from LSTM and reference dataset ('LSTM-extra-SWE-  
 727 REF'). All the LSTM predictions are generated from the model presented in section 4,  
 728 using the SWE fraction as the target. 'LSTM-in-situ' uses the historical maximum SWE  
 729 at each SNOTEL station to transform back to the SWE depth, using the nearest grid-  
 730 MET forcing for each SNOTEL station. Both the 'LSTM-extra-FRAC' and 'LSTM-extra-  
 731 SWE-REF' are estimates where the model is run at each UA grid point using the near-  
 732 est gridMET forcing and the nearest grid point to the SNOTEL station is then selected  
 733 for evaluation. 'LSTM-extra-fraction' uses LSTM-generated SWE fraction, with eval-  
 734 uation performed on SWE fraction from each SNOTEL station, whereas 'LSTM-extra-  
 735 SWE-REF' incorporates the historical maximum SWE from reference datasets. As shown  
 736 in Table 4, LSTM SWE generated at UA grid points leads to a significant NSE drop of  
 737 0.05-0.06 (when predicting fraction) or 0.07-0.10 (when predicting absolute SWE) and  
 738 a corresponding increase in MAE. This suggests that significant errors emerge in the gen-

**Table 4.** Tabulated model comparison for prediction of SWE at SNOTEL stations in the Rocky Mountains using different interpolation methods. The top table shows performance scores on dates when observed SWE is greater than zero, while the bottom table shows the whole evaluation period (from 2008 to 2018). The best scores for each metric are shown in bold font.

Nonzero SWE	Median NSE	Median MAE (mm)	Median RMSE (mm)
LSTM-in-situ	<b>0.802</b>	<b>41.88</b>	<b>58.28</b>
UA	0.775	45.09	65.44
UCLA	0.560	70.38	98.82
LSTM-extra-FRAC	0.743	-	-
LSTM-extra-SWE-UA	0.700	57.60	77.56
LSTM-extra-SWE-UCLA	0.600	63.71	84.88
Whole Period	Median NSE	Median MAE (mm)	Median RMSE (mm)
LSTM-in-situ	<b>0.891</b>	<b>25.54</b>	<b>46.32</b>
UA	0.861	25.66	49.50
UCLA	0.727	47.23	78.95
LSTM-extra-FRAC	0.843	-	-
LSTM-extra-SWE-UA	0.824	35.63	60.76
LSTM-extra-SWE-UCLA	0.772	39.59	68.00
Data Evaluated			
LSTM-in-situ	gridMET nearest to SNOTEL stations, max SWE from SNOTEL stations		
LSTM-extra-FRAC	gridMET nearest to UA grid points		
LSTM-extra-SWE-REF	gridMET nearest to REF grid points, max SWE from reference dataset		

eration of gridded SWE products when interpolating quantities among grids, even those at a similar resolution, and so interpolation should be performed sparingly. Note that the UA performance in this test is unsurprising since SNOTEL data is directly assimilated into the UA product, and so the nearest UA data point is likely to be strongly coupled to the SNOTEL station.

As seen in Table 1, all the DL models obtain higher NSE values than the SNOW-17 model. In Section 3.3, it was shown that the DL models benefit from training with many SNOTEL stations; however, the SNOW-17 model, which is tuned separately for each station, relies on a set of equations to prescribe the relevant physical processes and a much smaller set of tuning parameters. The difference in performance does not appear to arise from limited inputs: although the SNOW-17 model only takes precipitation, temperature, latitude and elevation as inputs, as shown in Table 3, a DL-reduced model with only these inputs (and others permuted) still yields a whole period median NSE of 0.874 versus SNOW-17's 0.722. Of course, in the permuted model the additional variables are not removed, only permuted, and so a fair comparison would require us to train an additional model that only uses these inputs. Doing so yields a whole period median NSE of 0.846, higher than SNOW-17 but lower than the full model. This result suggests there is still substantial room for improvement in the SNOW-17 model, although we do acknowledge that more modern process-based models are likely to yield better performance. A concerted effort to replace individual processes with SNOW-17 with data-driven models could pinpoint areas of particular deficiency, though such work is beyond the scope of this study, but an important point in how ML can also inform physics-based model development.

762 Although the extrapolated SWE estimations generated with our fractional SWE  
 763 model require the use of maximum historical SWE from a reference dataset to obtain  
 764 SWE magnitude, fractional values can still provide valuable insights via some metrics,  
 765 such as snow onset and melt date (see Rhoades, Jones, and Ullrich (2018)). Consequently,  
 766 one could use these metrics to quantify some features of snowpack response under cli-  
 767 mate change. While some past efforts have sought to address climate change impact on  
 768 snowpack with climate model simulations, the grid spacing employed in climate mod-  
 769 els is relatively generally coarse (e.g., 28 km in Rhoades, Ullrich, and Zarzycki (2018)),  
 770 and so is largely unable to capture the most rugged topography and shadow casting por-  
 771 tions of mountainous areas and their influence on the local meteorology. Given the de-  
 772 velopment of downscaled climate simulations (e.g., 1/16-degree LOCA dataset by (Pierce  
 773 et al., 2014) and 4-km MACA dataset by Abatzoglou and Brown (2012)), our DL mod-  
 774 els could be used for SWE ensemble projections at much higher spatial resolution. Since  
 775 the frigid temperatures of high-elevation regions provide a buffer against climate change,  
 776 it is essential that SWE models operate at spatial scales fine enough to resolve moun-  
 777 tain peaks. The necessary and sufficient spatial resolution, which is likely mountain range  
 778 dependent, to get convergence in mountain range or basin-average peak SWE could be  
 779 investigated in future work.

## 780 6 Conclusions

781 Previous studies have investigated and demonstrated that DL models are useful  
 782 for Earth system applications. The present work investigates three DL models for SWE  
 783 prediction over the Western US, with a focus on the Rocky Mountain region. The LSTM  
 784 model, which is particularly well-suited to time-series tasks, achieves the best accuracy  
 785 for SWE prediction in our experiments. The TCNN, another DL model, mimics the tem-  
 786 poral dependency with stacked 1-D CNN layers, but without inherent states like LSTM  
 787 model, its performance was somewhat worse. Attention models are also promising DL  
 788 methods and have become widespread in their use for time-series tasks, especially for nat-  
 789 ural language processing (NLP). Despite also demonstrating some capacity for predict-  
 790 ing SWE, results from the Attention model were similar to the TCNN. Besides these typ-  
 791 ical DL models, there have been efforts to combine different types of sequential layers  
 792 or blocks in a hybrid model, as shown in Xu et al. (2020) and Y. Chen et al. (2020). Al-  
 793 ternate architectures of DL models, including hybrid forms of the models discussed above,  
 794 hold promise for further improvements, but are left for investigation in future work.

795 Compared with the SNOW-17 process-based model and select reference datasets,  
 796 DL models can achieve higher accuracy (in terms of NSE), when estimating in-situ SNO-  
 797 TEL observations. By leveraging acceleration from GPUs, the DL model training time  
 798 is reasonable and the inference is fast. Given the important role that SWE has in the  
 799 mountainous hydrological cycle, DL models show promise for use in operational forecast-  
 800 ing and long-term projection. The computational speed of DL models also allows one  
 801 to generate an ensemble of SWE predictions through perturbations of the initial weights  
 802 of the model, enabling probabilistic SWE predictions.

803 A permutation-based method is used to better interpret the proposed DL model.  
 804 Precipitation and elevation are shown to be the two dominant variables for SWE pre-  
 805 diction, consistent with our physical understanding of snowpack dynamics. Although this  
 806 result is intuitive, this analysis is useful for building trust in the ‘black box’ ML-based  
 807 model before employing it for real applications. We caution that any conclusions drawn  
 808 from this interpretation could be sensitive to strong correlations among input variables.  
 809 In future work, we would like to examine methods that could eliminate these input cor-  
 810 relations. For example, one could reconstruct a set of orthogonal input variables from  
 811 the original inputs using principal component analysis. These orthogonal variables would  
 812 contain the same information as the original inputs, which preserves the accuracy of the  
 813 DL models, and the orthogonality would simplify the interpretation process. Nonethe-

814 less, the interpretation will be drawn from the reconstructed variables, which are linear  
 815 combinations of original inputs and may not represent any real physical features.

816 Although in-situ estimates of SWE are useful for particular applications, spatiotem-  
 817 porally continuous SWE predictions are needed for a wider range of applications. As a  
 818 proof of concept, we apply the trained DL model to generate a gridded SWE estimation  
 819 across the Rocky Mountains. A major constraint for our DL model is that most in-situ  
 820 estimates of SWE are provided at mid-to-high elevations at discrete points throughout  
 821 the Rocky Mountains. Therefore, the extrapolation problem for our DL model is par-  
 822 ticularly pronounced when we apply our model to a wider spatial area where the sta-  
 823 tistical properties learned from the in-situ measurements might not hold (e.g., lower el-  
 824 evations). Without additional training data, our extrapolation results prove that we can  
 825 generalize the DL models by altering the prediction from an absolute SWE depth to its  
 826 seasonality. With this transformation, the target prediction becomes an elevation-invariant  
 827 quantity that can be generalized to low-elevation areas, an approach also used for cli-  
 828 mate model emulation in Beucler, Pritchard, Yuval, et al. (2021). To overcome the ex-  
 829 trapulation problem without any loss of information (or transformation), the DL mod-  
 830 els would either need more training data in low-elevation areas (e.g., satellite images)  
 831 or incorporate physical constraints into their architectures (Kashinath et al., 2021).

832 A limitation of our study is that it mainly focuses on the use of data-driven mod-  
 833 els and does not incorporate physical constraints. One opportunity for future work would  
 834 be to add mass balance into the model, as with the model described in Hoedt et al. (2021).  
 835 These physical constraints could improve the physical interpretability of these models,  
 836 as well. It should be noted that although we used the UA and UCLA datasets as ref-  
 837 erences for extrapolation, their accuracy cannot be directly evaluated. Indeed, differences  
 838 between these two datasets are observed from both grid point-wise NSE values and area-  
 839 mean climatology time series over the Rocky Mountains, indicative of the uncertainties  
 840 in these datasets. Additionally, the UCLA dataset provides not only the mean SWE es-  
 841 timations, but also other statistics (such as median and quantiles). With DL models, such  
 842 distributions could be generated along with point estimations, which would allow for the  
 843 quantification of uncertainty and variability, which is useful for applications such as Earth  
 844 system model development. Finally, it is clear that the mean squared error-based loss  
 845 function employed in DL model training often underestimates extreme values. Gener-  
 846 ative adversarial models now being explored for Earth system modeling (Manepalli et  
 847 al., 2019; Pan et al., 2021) could allow for extremes to be better captured using both se-  
 848 quential models and adversarial loss.

## 849 Appendix A SNOW-17 Parameters

850 The following parameters are tuned for the SNOW-17 model. The snow-rain par-  
 851 tition uses a linear transition scheme, which involves PXTEMP1 and PXTEMP2, while  
 852 PXTEMP is only used for the rain temperature for the energy budget.

## 853 Appendix B Hyperparameter search

854 Hyperparameters are set based on a grid search over a range of parameter values.  
 855 The search space for these values is provided here. Each candidate model is trained with  
 856 the training data and evaluated with the validation period. The model results in the best  
 857 NSE value is taken as the optimal hyperparameter setting. For the Attention model, it  
 858 is required that the embedding size should be divisible by the number of heads. So in  
 859 the following grid search, embedding size is the product of embedding size ratio and num-  
 860 ber of heads.

**Table A1.** SNOW-17 parameters

Parameter	Description	Unit	Range
SCF	Gage catch deficit multiplying factor		0.9-1.2
MFMAX	Maximum melt factor during non-rain periods	$\text{mm} \cdot ^\circ\text{C} \cdot 6\text{hr}^{-1}$	0.5-1.3
MFMIN	Minimum melt factor during non-rain periods	$\text{mm} \cdot ^\circ\text{C} \cdot 6\text{hr}^{-1}$	0.1-0.6
UADJ	Average wind function during rain-on-snow periods	$\text{mm} \cdot \text{mb}^{-1}$	0.05-0.2
PXTEMP	Temperature that separates rain and snow	$^\circ\text{C}$	0.0-2.0
PXTEMP1	Lower limit temperature dividing transition from snow	$^\circ\text{C}$	-2.0-0.0
PXTEMP2	Upper limit temperature dividing rain from transition	$^\circ\text{C}$	0.0-4.0

**Table B1.** Hyperparameter search candidates for all DL models.

LSTM					
Hidden states	64	128	256	512	
TCNN					
Blocks	4	5	6		
Kernel size	7	9			
Number of kernels	16	32	64		
Attention					
Heads	8	16			
Embedding size ratio	1	2			
Attention layers	2	3	4		
Forward dimension	16	32	64		

We further tested several Attention models with 32 heads. The models generally have similar performance to the 16-head models, but take a much longer time for training. With such a small increment in performance, we decided to stop searching at 16 heads.

#### Acknowledgments

This study was funded by the Director, Office of Science, Office of Biological and Environmental Research of the U.S. Department of Energy Regional and Global Climate Modeling Program (RGCM) “the Calibrated and Systematic Characterization, Attribution and Detection of Extremes (CASCADE)” Science Focus Area (award no. DE-AC02-05CH11231) and the “An Integrated Evaluation of the Simulated Hydroclimate System of the Continental US” project (award no. DE-SC0016605). We would like to thank MetroIT at UC Davis for the Tempest GPU cluster. We also thank the Computational and Information System Lab for access to the Casper cluster through the Advanced Study Program at the National Center for Atmospheric Research (NCAR). We acknowledge the helpful discussion with Chaopeng Shen, Wen-Ping Tsai from Pennsylvania State University, David John Gagne from NCAR, and Chris Paciorek from Lawrence Berkeley National Laboratory.

The deep learning model code can be found at <https://github.com/ShihengDuan/code-SWE>. Our predictions for SNOTEL stations, extrapolation over the Rocky Mountains along with the necessary code can be accessed at DOI10.5281/zenodo.6419931 (S. Duan et al., 2022). SNOTEL SWE observations can be accessed at <https://www.nrcs.usda.gov/wps/portal/wcc/home/>. GridMET atmospheric data is available at <https://>

882 [www.climatologylab.org/gridmet.html](http://www.climatologylab.org/gridmet.html). PRISM dataset is provided by PRISM Cli-  
 883 mate Group at: <https://prism.oregonstate.edu>. DEM data is provided by USGS  
 884 can available through Microsoft Planetary Computer at <https://planetarycomputer.microsoft.com>.

886 This document was prepared as an account of work sponsored by the United States  
 887 Government. While this document is believed to contain correct information, neither the  
 888 United States Government nor any agency thereof, nor the Regents of the University of  
 889 California, nor any of their employees, makes any warranty, express or implied, or as-  
 890 sumes any legal responsibility for the accuracy, completeness, or usefulness of any infor-  
 891 mation, apparatus, product, or process disclosed, or represents that its use would not  
 892 infringe privately owned rights. Reference herein to any specific commercial product, pro-  
 893 cess, or service by its trade name, trademark, manufacturer, or otherwise, does not nec-  
 894 essarily constitute or imply its endorsement, recommendation, or favoring by the United  
 895 States Government or any agency thereof, or the Regents of the University of Califor-  
 896 nia. The views and opinions of authors expressed herein do not necessarily state or re-  
 897 flect those of the United States Government or any agency thereof or the Regents of the  
 898 University of California.

## 899 References

- 900 Abatzoglou, J. T. (2013). Development of gridded surface meteorological data for  
 901 ecological applications and modelling. *International Journal of Climatology*,  
 902 33(1), 121–131.
- 903 Abatzoglou, J. T., & Brown, T. J. (2012). A comparison of statistical downscaling  
 904 methods suited for wildfire applications. *International journal of climatology*,  
 905 32(5), 772–780.
- 906 Addor, N., Newman, A. J., Mizukami, N., & Clark, M. P. (2017). The camels data  
 907 set: catchment attributes and meteorology for large-sample studies. *Hydrology*  
 908 and *Earth System Sciences*, 21(10), 5293–5313.
- 909 Anderson, E. (2006). *Snow accumulation and ablation model – snow-17*. (<https://www.weather.gov/media/owp/oh/hrl/docs/22snow17.pdf>)
- 910 Anderson, E. A. (1973). *National weather service river forecast system: Snow accu-*  
 911 *mulation and ablation model* (Vol. 17). US Department of Commerce, National  
 912 Oceanic and Atmospheric Administration ....
- 913 Anderson, E. A. (1976). *A point energy and mass balance model of a snow cover*.  
 914 Stanford University.
- 915 Bahdanau, D., Cho, K., & Bengio, Y. (2014). Neural machine translation by jointly  
 916 learning to align and translate. *arXiv preprint arXiv:1409.0473*.
- 917 Bai, S., Kolter, J. Z., & Koltun, V. (2018). An empirical evaluation of generic  
 918 convolutional and recurrent networks for sequence modeling. *arXiv preprint*  
 919 *arXiv:1803.01271*.
- 920 Balestrieri, R., Pesenti, J., & LeCun, Y. (2021). Learning in high dimension always  
 921 amounts to extrapolation. *arXiv preprint arXiv:2110.09485*.
- 922 Barnes, E. A., Toms, B., Hurrell, J. W., Ebert-Uphoff, I., Anderson, C., & Ander-  
 923 son, D. (2020). Indicator patterns of forced change learned by an artificial  
 924 neural network. *Journal of Advances in Modeling Earth Systems*, 12(9),  
 925 e2020MS002195.
- 926 Berghuijs, W. R., Harrigan, S., Molnar, P., Slater, L. J., & Kirchner, J. W. (2019).  
 927 The relative importance of different flood-generating mechanisms across eu-  
 928 rope. *Water Resources Research*, 55(6), 4582–4593.
- 929 Beucler, T., Pritchard, M., Rasp, S., Ott, J., Baldi, P., & Gentine, P. (2021). Enforc-  
 930 ing analytic constraints in neural networks emulating physical systems. *Physi-*  
 931 *cal Review Letters*, 126(9), 098302.
- 932 Beucler, T., Pritchard, M., Yuval, J., Gupta, A., Peng, L., Rasp, S., ... others

- (2021). Climate-invariant machine learning. *arXiv preprint arXiv:2112.08440*.
- Blöschl, G. (1999). Scaling issues in snow hydrology. *Hydrological processes*, 13(14-15), 2149–2175.
- Böhner, J., & Antonić, O. (2009). Land-surface parameters specific to topoclimatology. *Developments in soil science*, 33, 195–226.
- Breiman, L. (1996). Bagging predictors. *Machine learning*, 24(2), 123–140.
- Broxton, P. D., Dawson, N., & Zeng, X. (2016). Linking snowfall and snow accumulation to generate spatial maps of swe and snow depth. *Earth and Space Science*, 3(6), 246–256.
- Chen, X., Leung, L. R., Gao, Y., & Liu, Y. (2021). Response of us west coast mountain snowpack to local sea surface temperature perturbations: insights from numerical modeling and machine learning. *Journal of Hydrometeorology*, 22(4), 1045–1062.
- Chen, Y., Dai, X., Liu, M., Chen, D., Yuan, L., & Liu, Z. (2020). Dynamic convolution: Attention over convolution kernels. In *Proceedings of the ieee/cvf conference on computer vision and pattern recognition* (pp. 11030–11039).
- Civitarese, D. S., Szwarcman, D., Zadrozny, B., & Watson, C. (2021). Extreme precipitation seasonal forecast using a transformer neural network. *arXiv preprint arXiv:2107.06846*.
- Cristea, N. C., Breckheimer, I., Raleigh, M. S., HilleRisLambers, J., & Lundquist, J. D. (2017). An evaluation of terrain-based downscaling of fractional snow covered area data sets based on lidar-derived snow data and orthoimagery. *Water Resources Research*, 53(8), 6802–6820.
- Daly, C., Halbleib, M., Smith, J. I., Gibson, W. P., Doggett, M. K., Taylor, G. H., ... Pasteris, P. P. (2008). Physiographically sensitive mapping of climatological temperature and precipitation across the conterminous united states. *International Journal of Climatology: a Journal of the Royal Meteorological Society*, 28(15), 2031–2064.
- Devlin, J., Chang, M.-W., Lee, K., & Toutanova, K. (2018). Bert: Pre-training of deep bidirectional transformers for language understanding. *arXiv preprint arXiv:1810.04805*.
- Duan, Q., Gupta, V. K., & Sorooshian, S. (1993). Shuffled complex evolution approach for effective and efficient global minimization. *Journal of optimization theory and applications*, 76(3), 501–521.
- Duan, Q., Sorooshian, S., & Gupta, V. K. (1994). Optimal use of the sce-ua global optimization method for calibrating watershed models. *Journal of hydrology*, 158(3-4), 265–284.
- Duan, S., Ullrich, P., Risser, M., & Rhoades, A. (2022). *Historical daily snow water equivalent (swe) estimations over the western us and the rocky mountains*. Zenodo. Retrieved from <https://zenodo.org/record/6419930> doi: 10.5281/ZENODO.6419930
- Duan, S., Ullrich, P., & Shu, L. (2020). Using convolutional neural networks for streamflow projection in california. *Frontiers in Water*, 2, 28.
- Fang, K., Kifer, D., Lawson, K., Feng, D., & Shen, C. (2022). The data synergy effects of time-series deep learning models in hydrology. *Water Resources Research*, 58(4), e2021WR029583.
- Fang, Y., Liu, Y., & Margulis, S. A. (2022). A western united states snow reanalysis dataset over the landsat era from water years 1985 to 2021. *Scientific Data*, 9(1), 677.
- Feng, D., Beck, H., Lawson, K., & Shen, C. (2022). The suitability of differentiable, learnable hydrologic models for ungauged regions and climate change impact assessment. *Hydrology and Earth System Sciences Discussions*, 1–28.
- Feng, D., Fang, K., & Shen, C. (2020). Enhancing streamflow forecast and extracting insights using long-short term memory networks with data integration at continental scales. *Water Resources Research*, 56(9), e2019WR026793.

- 989 Gagne II, D. J., Haupt, S. E., Nychka, D. W., & Thompson, G. (2019). Inter-  
 990     prettable deep learning for spatial analysis of severe hailstorms. *Monthly*  
 991      *Weather Review*, 147(8), 2827–2845.
- 992 Hatchett, B. J., Rhoades, A. M., & McEvoy, D. J. (2022). Monitoring the daily  
 993      evolution and extent of snow drought. *Natural Hazards and Earth System Sci-*  
 994      *ences*, 22(3), 869–890.
- 995 He, K., Zhang, X., Ren, S., & Sun, J. (2016). Deep residual learning for image  
 996      recognition. In *Proceedings of the ieee conference on computer vision and pat-*  
 997      *tern recognition* (pp. 770–778).
- 998 He, M., Hogue, T. S., Franz, K. J., Margulis, S. A., & Vrugt, J. A. (2011a). Charac-  
 999      terizing parameter sensitivity and uncertainty for a snow model across hydro-  
 1000      climatic regimes. *Advances in Water Resources*, 34(1), 114–127.
- 1001 He, M., Hogue, T. S., Franz, K. J., Margulis, S. A., & Vrugt, J. A. (2011b). Cor-  
 1002      ruption of parameter behavior and regionalization by model and forcing data  
 1003      errors: A bayesian example using the snow17 model. *Water Resources Re-*  
 1004      *search*, 47(7).
- 1005 Hochreiter, S., & Schmidhuber, J. (1997). Long short-term memory. *Neural compu-*  
 1006      *tation*, 9(8), 1735–1780.
- 1007 Hoedt, P.-J., Kratzert, F., Klotz, D., Halmich, C., Holzleitner, M., Nearing, G.,  
 1008      ... Klambauer, G. (2021). Mc-lstm: Mass-conserving lstm. *arXiv preprint*  
 1009      *arXiv:2101.05186*.
- 1010 Jennings, K., Winchell, T. S., Livneh, B., & Molotch, N. P. (2018). Spatial variation  
 1011      of the rain–snow temperature threshold across the Northern Hemisphere. *Na-*  
 1012      *ture Communications*, 9(1). doi: 10.1038/s41467-018-03629-7
- 1013 Kashinath, K., Mustafa, M., Albert, A., Wu, J., Jiang, C., Esmaeilzadeh, S., ...  
 1014      others (2021). Physics-informed machine learning: case studies for weather  
 1015      and climate modelling. *Philosophical Transactions of the Royal Society A*,  
 1016      379(2194), 20200093.
- 1017 King, F., Erler, A. R., Frey, S. K., & Fletcher, C. G. (2020). Application of ma-  
 1018      chine learning techniques for regional bias correction of snow water equivalent  
 1019      estimates in ontario, canada. *Hydrology and Earth System Sciences*, 24(10),  
 1020      4887–4902.
- 1021 Kingma, D. P., & Ba, J. (2014). Adam: A method for stochastic optimization. *arXiv*  
 1022      *preprint arXiv:1412.6980*.
- 1023 Kratzert, F., Klotz, D., Shalev, G., Klambauer, G., Hochreiter, S., & Nearing, G.  
 1024      (2019a). Benchmarking a catchment-aware long short-term memory network  
 1025      (lstm) for large-scale hydrological modeling. *arXiv preprint arXiv:1907.08456*.
- 1026 Kratzert, F., Klotz, D., Shalev, G., Klambauer, G., Hochreiter, S., & Nearing, G.  
 1027      (2019b). Towards learning universal, regional, and local hydrological behaviors  
 1028      via machine learning applied to large-sample datasets. *Hydrology and Earth*  
 1029      *System Sciences*, 23(12), 5089–5110.
- 1030 Lea, C., Flynn, M. D., Vidal, R., Reiter, A., & Hager, G. D. (2017). Temporal  
 1031      convolutional networks for action segmentation and detection. In *proceedings of*  
 1032      *the ieee conference on computer vision and pattern recognition* (pp. 156–165).
- 1033 Lees, T., Buechel, M., Anderson, B., Slater, L., Reece, S., Coxon, G., & Dadson,  
 1034      S. J. (2021). Benchmarking data-driven rainfall-runoff models in great britain:  
 1035      A comparison of lstm-based models with four lumped conceptual models.  
 1036      *Hydrology and Earth System Sciences Discussions*, 1–41.
- 1037 Lin, T., Wang, Y., Liu, X., & Qiu, X. (2021). A survey of transformers. *arXiv*  
 1038      *preprint arXiv:2106.04554*.
- 1039 Livneh, B., & Badger, A. M. (2020). Drought less predictable under declining future  
 1040      snowpack. *Nature Climate Change*, 10(5), 452–458.
- 1041 Livneh, B., Bohn, T. J., Pierce, D. W., Munoz-Arriola, F., Nijssen, B., Vose, R., ...  
 1042      Brekke, L. (2015). A spatially comprehensive, hydrometeorological data set for  
 1043      mexico, the us, and southern canada 1950–2013. *Scientific data*, 2(1), 1–12.

- 1044 Manepalli, A., Albert, A., Rhoades, A., Feldman, D., & Jones, A. D. (2019). Emulating numeric hydroclimate models with physics-informed cgans. In *Agu fall meeting 2019*.
- 1045 Margulis, S. A., Liu, Y., & Baldo, E. (2019). A joint landsat-and modis-based reanalysis approach for midlatitude montane seasonal snow characterization. *Frontiers in Earth Science*, 7, 272.
- 1046
- 1047 McCrary, R. R., McGinnis, S., & Mearns, L. O. (2017). Evaluation of snow water equivalent in narccap simulations, including measures of observational uncertainty. *Journal of Hydrometeorology*, 18(9), 2425 - 2452. Retrieved from <https://journals.ametsoc.org/view/journals/hydr/18/9/jhm-d-16-0264.1.xml> doi: <https://doi.org/10.1175/JHM-D-16-0264.1>
- 1048 McGovern, A., Lagerquist, R., Gagne, D. J., Jergensen, G. E., Elmore, K. L., Homeyer, C. R., & Smith, T. (2019). Making the black box more transparent: Understanding the physical implications of machine learning. *Bulletin of the American Meteorological Society*, 100(11), 2175–2199.
- 1049
- 1050 Meyal, A. Y., Versteeg, R., Alper, E., Johnson, D., Rodzianko, A., Franklin, M., & Wainwright, H. (2020). Automated cloud based long short-term memory neural network based swe prediction. *Frontiers in Water*, 2.
- 1051
- 1052 Nash, J. E., & Sutcliffe, J. V. (1970). River flow forecasting through conceptual models part i—a discussion of principles. *Journal of hydrology*, 10(3), 282–290.
- 1053
- 1054 Ntokas, K. F., Odry, J., Boucher, M.-A., & Garnaud, C. (2021). Investigating ann architectures and training to estimate snow water equivalent from snow depth. *Hydrology and Earth System Sciences*, 25(6), 3017–3040.
- 1055
- 1056 Odry, J., Boucher, M., Cantet, P., Lachance-Cloutier, S., Turcotte, R., & St-Louis, P. (2020). Using artificial neural networks to estimate snow water equivalent from snow depth. *Canadian Water Resources Journal/Revue canadienne des ressources hydriques*, 45(3), 252–268.
- 1057
- 1058 Pan, B., Anderson, G. J., Goncalves, A., Lucas, D. D., Bonfils, C. J., Lee, J., ...
- 1059 Ma, H.-Y. (2021). Learning to correct climate projection biases. *Journal of Advances in Modeling Earth Systems*, 13(10), e2021MS002509.
- 1060
- 1061 Paszke, A., Gross, S., Massa, F., Lerer, A., Bradbury, J., Chanan, G., ... Chintala, S. (2019). Pytorch: An imperative style, high-performance deep learning library. In H. Wallach, H. Larochelle, A. Beygelzimer, F. d'Alché-Buc, E. Fox, & R. Garnett (Eds.), *Advances in neural information processing systems 32* (pp. 8024–8035). Curran Associates, Inc. Retrieved from <http://papers.neurips.cc/paper/9015-pytorch-an-imperative-style-high-performance-deep-learning-library.pdf>
- 1062
- 1063 Pierce, D. W., Cayan, D. R., & Thrasher, B. L. (2014). Statistical downscaling using localized constructed analogs (loca). *Journal of Hydrometeorology*, 15(6), 2558–2585.
- 1064
- 1065 Raleigh, M. S., & Lundquist, J. D. (2012). Comparing and combining swe estimates from the snow-17 model using prism and swe reconstruction. *Water Resources Research*, 48(1).
- 1066
- 1067 Rhoades, A. M., Hatchett, B. J., Risser, M. D., Collins, W. D., Bambach, N. E., Huning, L. S., ... others (2022). Asymmetric emergence of low-to-no snow in the midlatitudes of the american cordillera. *Nature Climate Change*, 1–9.
- 1068
- 1069 Rhoades, A. M., Jones, A. D., & Ullrich, P. A. (2018). Assessing mountains as natural reservoirs with a multimetric framework. *Earth's Future*, 6(9), 1221–1241.
- 1070
- 1071 Rhoades, A. M., Ullrich, P. A., & Zarzycki, C. M. (2018). Projecting 21st century snowpack trends in western usa mountains using variable-resolution cesm. *Climate Dynamics*, 50(1), 261–288.
- 1072
- 1073 Roberts, D. W., & Cooper, S. V. (1989). Concepts and techniques of vegetation mapping. *Land classifications based on vegetation: applications for resource management*, 90–96.
- 1074
- 1075
- 1076
- 1077
- 1078
- 1079
- 1080
- 1081
- 1082
- 1083
- 1084
- 1085
- 1086
- 1087
- 1088
- 1089
- 1090
- 1091
- 1092
- 1093
- 1094
- 1095
- 1096
- 1097
- 1098

- 1099 Serreze, M. C., Clark, M. P., Armstrong, R. L., McGinnis, D. A., & Pulwarty, R. S.  
 1100 (1999). Characteristics of the western united states snowpack from snowpack  
 1101 telemetry (snotel) data. *Water Resources Research*, 35(7), 2145–2160.
- 1102 Siirila-Woodburn, E. R., Rhoades, A. M., Hatchett, B. J., Huning, L. S., Szinai, J.,  
 1103 Tague, C., ... others (2021). A low-to-no snow future and its impacts on water  
 1104 resources in the western united states. *Nature Reviews Earth & Environment*,  
 1105 2(11), 800–819.
- 1106 Simonyan, K., & Zisserman, A. (2014). Very deep convolutional networks for large-  
 1107 scale image recognition. *arXiv preprint arXiv:1409.1556*.
- 1108 Snauffer, A. M., Hsieh, W. W., Cannon, A. J., & Schnorbus, M. A. (2018). Im-  
 1109 proving gridded snow water equivalent products in british columbia, canada:  
 1110 multi-source data fusion by neural network models. *The Cryosphere*, 12(3),  
 1111 891–905.
- 1112 Szegedy, C., Liu, W., Jia, Y., Sermanet, P., Reed, S., Anguelov, D., ... Rabinovich,  
 1113 A. (2015). Going deeper with convolutions. In *Proceedings of the ieee confer-  
 1114 ence on computer vision and pattern recognition* (pp. 1–9).
- 1115 Tay, Y., Dehghani, M., Bahri, D., & Metzler, D. (2020). Efficient transformers: A  
 1116 survey. *arXiv preprint arXiv:2009.06732*.
- 1117 Toms, B. A., Barnes, E. A., & Ebert-Uphoff, I. (2020). Physically interpretable neu-  
 1118 ral networks for the geosciences: Applications to earth system variability. *Jour-  
 1119 nal of Advances in Modeling Earth Systems*, 12(9), e2019MS002002.
- 1120 Tsymbal, A. (2004). The problem of concept drift: definitions and related work.  
 1121 *Computer Science Department, Trinity College Dublin*, 106(2), 58.
- 1122 Vaswani, A., Shazeer, N., Parmar, N., Uszkoreit, J., Jones, L., Gomez, A. N.,  
 1123 ... Polosukhin, I. (2017). Attention is all you need. *arXiv preprint  
 1124 arXiv:1706.03762*.
- 1125 Wang, X., Kondratyuk, D., Christiansen, E., Kitani, K. M., Alon, Y., & Eban, E.  
 1126 (2021). *Wisdom of committees: An overlooked approach to faster and more  
 1127 accurate models*.
- 1128 Wang, Y.-H., Gupta, H. V., Zeng, X., & Niu, G.-Y. (2022). Exploring the po-  
 1129 tential of long short-term memory networks for improving understanding of  
 1130 continental-and regional-scale snowpack dynamics. *Water Resources Research*,  
 1131 58(3), e2021WR031033.
- 1132 Wunsch, A., Liesch, T., & Broda, S. (2021). Groundwater level forecasting with  
 1133 artificial neural networks: a comparison of long short-term memory (lstm),  
 1134 convolutional neural networks (cnns), and non-linear autoregressive networks  
 1135 with exogenous input (narx). *Hydrology and Earth System Sciences*, 25(3),  
 1136 1671–1687.
- 1137 Xiang, Z., Yan, J., & Demir, I. (2020). A rainfall-runoff model with lstm-  
 1138 based sequence-to-sequence learning. *Water resources research*, 56(1),  
 1139 e2019WR025326.
- 1140 Xu, G., Ren, T., Chen, Y., & Che, W. (2020). A one-dimensional cnn-lstm model  
 1141 for epileptic seizure recognition using eeg signal analysis. *Frontiers in Neuro-  
 1142 science*, 14, 1253.
- 1143 Yan, J., Mu, L., Wang, L., Ranjan, R., & Zomaya, A. Y. (2020). Temporal convolu-  
 1144 tional networks for the advance prediction of enso. *Scientific reports*, 10(1), 1–  
 1145 15.
- 1146 Ye, F., Hu, J., Huang, T.-Q., You, L.-J., Weng, B., & Gao, J.-Y. (2021). Trans-  
 1147 former for ei niño-southern oscillation prediction. *IEEE Geoscience and Re-  
 1148 mote Sensing Letters*.
- 1149 Zeng, X., Broxton, P., & Dawson, N. (2018). Snowpack change from 1982 to 2016  
 1150 over conterminous united states. *Geophysical Research Letters*, 45(23), 12–  
 1151 940.